

# 10+ Years of GST: Collection of Science Publications (1999-2022)

## Contents

1. Fine Structure of the Quiet Sun Photosphere	2
2. Ellerman Bombs	5
3. Small-scale Reconnection and Chromospheric Flows	7
4. Structure of Sunspots and Pores	11
5. Sunspot Oscillations	14
6. Evolution of Active Regions	17
7. Filaments and Prominences	17
8. Solar Flares	19
9. Instrumentation, Data Processing, Numerical Tools, and Machine Learning	22

<sup>1</sup> send comments to V. Yurchyshyn, [vasyl.yurchyshyn@njit.edu](mailto:vasyl.yurchyshyn@njit.edu)

## 1. FINE STRUCTURE OF THE QUIET SUN PHOTOSPHERE

Quiet sun photosphere – areas outside sunspot groups – occupies more than 80% of the entire solar surface. In spite of the fact that there is no strong and complex magnetic fields there, no flares, the undisturbed photosphere plays an important role in the evolution of the sun. In particular, fundamental problems of magnetic field generation can benefit a lot from an analysis of transport processes in the quiet sun zones, of turbulent diffusion, of magneto-convection processes in granulation. A solution of these problems drastically depends on high-resolution observations in both temporal and spatial domains. The GST contribution was well-timed and significant to make an insight into this field.

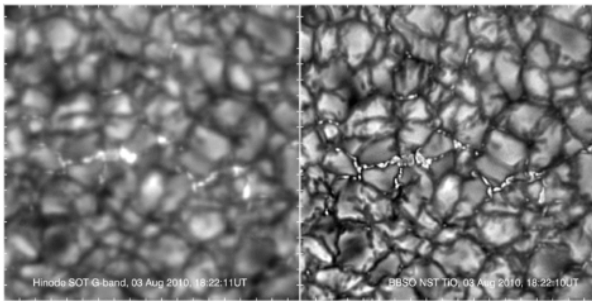


**Figure 1.** Left: Hinode G-band image obtained on 2010 August 3 at 18:22:11 UT (pixel size  $0''.109$ ). Right: GST TiO image obtained on 2010 August 3 at 18:22:10 UT (pixel size  $0''.0375$ ). Both images cover the same area of  $18''.8 \times 18''.8$  on the Sun. Adopted from [Abramenko et al. \(2010\)](#).

One of the most pronounced features of the quiet sun (QS) is the solar granulation. The GST can resolve very fine details of the granulation pattern. In case where Hinode/SOT detects one large BP, GST detects several separated BPs (1). Extended filigree features are clearly fragmented into separate BPs in GST images. The data showed ([Abramenko et al. 2012](#)) that along with the population of regular granules with the typical size of about 1000-1300 km and Gaussian size distribution, there is a distinct sub-population of mini-granules, which are dominant on spatial scales below 600 km (Figure 2). Their size is distributed as a power law with an index of -1.8 without predominant (average) scale and they are predominantly confined to the wide dark lanes between regular granules and often form chains and clusters (Figure 3). Interpretation of mini-granulation is that they are fragments of regular granules subjected to highly turbulent plasma flows in the intergranular lanes, where the intensity of turbulence is enhanced.

[Abramenko \(2016\)](#) explored fractal properties of solar granulation on scales below 600 km. The degree of multifractality found in various QS environments tends to increase as the magnetic fields become weaker. Since

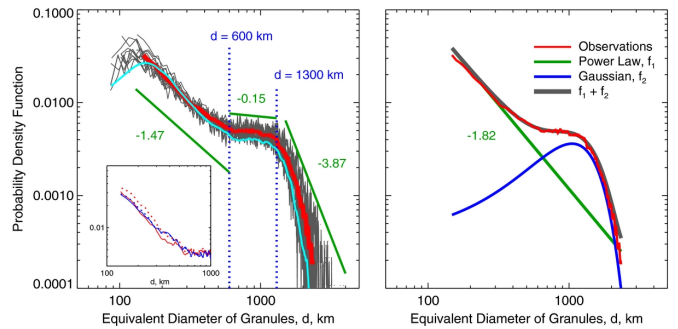


**Figure 2.** Left: PDFs of the granule equivalent diameter derived from 15 various detection runs (gray lines) overplotted with their average (thick red line). Positions where the averaged PDF rapidly changes its slope are denoted by the vertical blue dotted lines. Right: decomposition of the observed averaged PDF (red line) into two components: a power-law approximation ( $f_1$ , green line) and a Gaussian approximation ( $f_2$ , blue). Their sum ( $f_1 + f_2$ ) is plotted with the gray line. Adopted from [Abramenko et al. \(2012\)](#).

the multifractality on very small scales is associated with the fast turbulent dynamo action, the results show that most favorable conditions for the dynamo are encountered outside of the network fields within vast areas of weakest magnetic fields.

Another interesting and very important feature of the QS photosphere is the so called bright points (BPs) visible in various spectral bands and thought to be associated with vertical magnetic flux tubes. BPs are bright structures observed in darker intergranular lanes. It is generally agreed that they are brighter than the mean granular intensity because the dynamical equilibrium with the external gas is partly balanced by the magnetic field of what is commonly called a “flux tube”. Since the gas pressure inside the “tube” is lower, the measured radiance comes from deeper, hotter layers of the Sun. [Goode et al. \(2010\)](#) demonstrated for the first time that the photospheric plasma motion and magnetic fields are in equipartition over a wide dynamic range, and both cascade energy to ever-smaller scales according to classical Kolmogorov turbulence theory. What is obvious in this representative image is that BPs do not come in sheets as observations with lower spatial resolutions and simulations predict ([Goode et al. 2010](#)). In fact, we see no evidence of sheet-like structures in any of these observations covering the entire field of view over the duration of the data. So instead of an unstructured magnetic sheet in the dark lanes between granules, one might envision a turbulent “sheet” composed of separated, nearly vertical threads that are “washed out” at lower resolution, so as to appear continuous. [Andić et al. \(2011\)](#) found that observed BPs covered  $\sim 5\%$  of the solar surface and were not homogeneously distributed, while [Yurchyshyn et al. \(2010\)](#) reported that  $H\alpha$  BPs

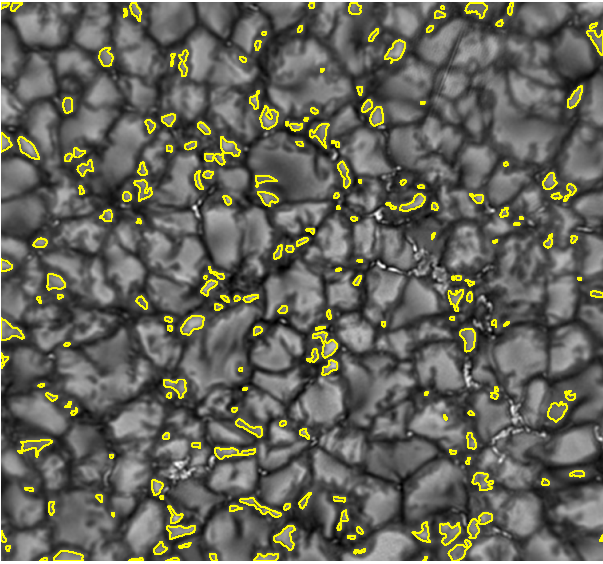


**Figure 3.** Image of solar granulation acquired at 18:30:30 UT on 2010 August 3 with overplotted contours of detected mini granules (i.e., structures of equivalent diameter less than 600 km). Adopted from [Abramenko et al. \(2012\)](#).

correspond to Ca II H BPs, which in turn are cospatial with G-band BPs (Figure 1).

[Hao et al. \(2020\)](#) performed spectral analysis of three typical photospheric BPs using H $\alpha$  and Ca II 8542 Å line profiles. It was found that the temperature enhancement in a BP is about 200-500 K. The total excess radiative energy of a typical BP is estimated to be  $1 \times 10^{27} - 2 \times 10^{27}$  erg, which can be regarded as the lower limit energy of the BPs. The radiation flux in the visible continuum for the BPs is about  $5.5 \times 10^{10} \text{ erg cm}^{-2} \text{ s}^{-1}$ . The results also indicate that the temperature in the atmosphere above BPs is close to that of a plage.

The diffraction limit (Rayleigh criterion) of GST at 700 nm is  $0''.11$ , which is essentially the same as the  $0''.12$  determined from speckle reconstruction of GST/TiO images. The largest “tubes” have a diameter about twice the diffraction limit and in these larger tubes one can detect a brightness gradient nearing the edge. Thus, in reality, they could be even narrower, brighter threads with more intense magnetic fields that appear round reflecting the telescope resolution at 700 nm. The distribution function of BP sizes extends to the diffraction limit of GST without saturation which means that the minimal size of BPs (and therefore, flux tubes) is not reached yet [Abramenko et al. \(2010\)](#).

Most of BPs normally disappear when the surrounding granules collide. [Abramenko et al. \(2010\)](#) reported that the majority of BPs are transient events reflecting the strong dynamics of the QS: 98.6% of BPs live less than 120 s. The lifetime distribution function follows a log-normal approximation for all BPs with lifetime ex-

ceeding 100 s. The longest registered lifetime was 44 min. This unexpected longevity of the bright points implies a deeper anchoring than predicted. [Andić et al. \(2011\)](#) found that BPs were detectable on the solar surface for 4.28 min on average. Frequently their collision creates a vortex into which BPs enter and spin around each other until they both disappear. Maps of the divergence and vorticity of transverse LCT velocities revealed large and well-defined cyclonic flows. [Andić et al. \(2010\)](#) reported that when the proper motion of the BPs is removed, more powerful oscillations can then be detected above them as compared to the areas without BPs.

A typical cadence of GST/TiO data is about 10-15 seconds, which offers an opportunity to explore dynamics of BPs (and, therefore, of flux tubes) and thus to probe the regime of turbulent diffusion in the photosphere. Turbulent magnetic diffusivity – a key parameter of the dynamo models and flux transport models – is the most poorly constrained parameter theoretically and observationally. In particular, the competition between diffusion and advection processes determines the solar cycle memory. The flux transport models usually adopt the regime of normal diffusion and, as a consequence, the same for all scales value of the diffusion coefficient. However, the regime might be an anomalous diffusion and the coefficient of turbulent diffusion may depend on scale (as spatial, so temporal). This will unavoidably affect the solar dynamo modeling.

A non-interrupted two-hour TiO data cube was used by [Abramenko et al. \(2011\)](#); [Goode et al. \(2012\)](#) to explore proper motion of BPs in a QS, a coronal hole (CH), and an AR plage area by analysing their mean-squared displacements as a function of time, the so-called displacement spectrum. Scaling of the displacement spectrum allowed authors to infer information on magnetic diffusivity. The spectral index  $\gamma$  of unity indicates normal diffusion and the scale-independent coefficient of turbulent diffusion, whereas  $\gamma > 1$  means the super-diffusion with the increasing with scale coefficient.

In [Abramenko et al. \(2011\)](#) it was shown that the regime of super-diffusivity is present in all analysed magnetic areas and visible down to smallest observable (spatial and temporal) scales. Super-diffusion increases from a plage area ( $\gamma = 1.48$ ) to a QS area ( $\gamma = 1.53$ ) to a CH ( $\gamma = 1.67$ ) (Figure 4). A comparison of displacement spectra derived from model and observed data on solar granulation [Abramenko et al. \(2011\)](#) showed that model data also exhibits super-diffusion with  $\gamma = 1.45$ , which is very close to that obtained from observations.

This differs considerably from the previously adopted normal diffusion with  $\gamma = 1$  and scale-independent coefficient of turbulent diffusion. The super-diffusion implies that the coefficient of turbulent diffusion changes in direct proportion to both temporal and spatial scales. For the minimum spatial scale (22 km) and minimum time scale (10 s), it is 22 and 19  $\text{km}^2 \text{ s}^{-1}$  for a CH and QS and 12  $\text{km}^2 \text{ s}^{-1}$  for a plage area. [Lepreti et al. \(2012\)](#)

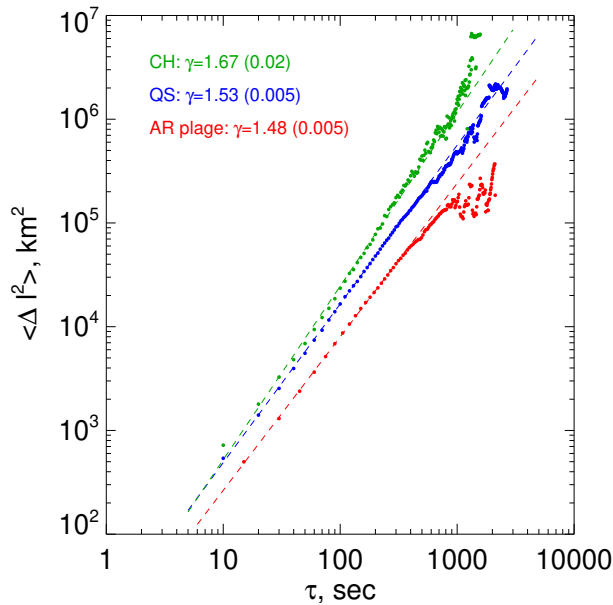


**Figure 4.** Displacement spectra determined for the CH data (green), QS area (blue), and AR plage area (red). Adopted from [Abramenko et al. \(2011\)](#).

extended this analysis using the pair-separation technique, which allowed authors to interpret the results in the framework of Batchelor theory, under the hypothesis that the observed range of timescales corresponds to a non-asymptotic regime in which the photospheric bright points keep the memory of their initial separations.

An analytical expression for the turbulent diffusion coefficient as a function of scales and  $\gamma$  was obtained in [Abramenko et al. \(2011\)](#), which was later used by many authors to explore diffusivity in the photosphere. As a whole, the above GST publications incited an interest to anomalous diffusion in solar surface magnetic fields and forced a deviation from a traditional standpoint on the reign of normal diffusion.

The high-cadence GST data also allowed [Abramenko et al. \(2013\)](#) to derive transverse velocity fields in the quiet sun photosphere, in particular, in a CH area. They determined the characteristic energy-containing length  $\lambda$  of the squared velocity and magnetic field fluctuations ( $u^2$  and  $b^2$ ) transverse to the mean magnetic field inside a CH at the base of the corona. The characteristic length scale defines the heating rate in the corona. They found that the characteristic length scale in the photosphere is approximately 1.5-50 times smaller than that adopted in previous models ( $3\text{-}30 \times 10^3$  km). These results provide a critical input parameter for current models of coronal heating and should yield an improved understanding of fast solar wind acceleration.

One of the widely recognized criterion for the quality of new data and of used approaches is a comparison

with corresponding results from theory and numerical simulations. The GST outcome for quiet sun photosphere was at least twice compared with the numerical simulations. Thus, [Kitiashvili et al. \(2013\)](#) compared the kinetic energy spectra on granular and sub-granular scales obtained from TiO data and 3D radiative magneto-hydrodynamic (MHD) numerical simulations. They found that the numerical simulations require high spatial resolution with a 10-25 km grid step in order to reproduce the inertial (Kolmogorov) turbulence range. The observational data require an averaging procedure to remove noise and potential instrumental artifacts. The resulting kinetic energy spectra reveal good agreement between the simulations and the observations.

[Abramenko and Yurchyshyn \(2020\)](#) using NIRSI data revealed thin flux tubes of 200-400 km in diameter and of 1000-2000 G field strength. When compared to the HMI spectra, the -1.2 slope of the NIRIS spectrum appears to be more extended into the short spatial range until the cut-off at 0.8-0.9 Mm, after which it continues with a steeper slope of -2.2. Kolmogorov turbulent cascade cannot account for more than 35 % of the total magnetic energy observed in the scale range of 3.5-0.3 Mm. The energy excess can be attributed to other mechanisms of field generation such as the local turbulent dynamo and magnetic superdiffusivity observed in an undisturbed photosphere that can slow down the rate of the Kolmogorov cascade leading to a shallower resulting spectrum.

[Kwak et al. \(2020\)](#) observed wave excitation by a new type of event: rapidly changing granules. They identified granules in the internetwork region that undergo rapid dynamic changes such as collapse (event 1), fragmentation (event 2), or submergence (event 3). In the photospheric images, these granules become significantly darker than neighboring granules. Following the granules' rapid changes, transient oscillations are detected in the photospheric and chromospheric layers. In the case of event 1, the dominant period of the oscillations is close to 4.2 min in the photosphere and 3.8 min in the chromosphere. Repetitive brightenings in the Ca II-0.5 Å raster images were observed at location of the rapidly changing granules that are considered the manifestation of shock waves. Data suggest that dynamic changes of granules can generate upward-propagating acoustic waves in the quiet Sun that ultimately develop into shocks.

[Ji et al. \(2021\)](#) studied quasi-periodic perturbations in time profiles of line of sight (LOS) magnetic fields in a solar plage. The perturbations were found to be associated with the enhancement of He I 10830 Å absorption in a moss region. The amplitudes of the magnetic perturbations are found to be proportional to magnetic field strength. Observational analysis also shows that, for the two regions with stronger and weaker magnetic field, the perturbations are always anti-phased. All findings show that the magnetic perturbations are actually

magneto-acoustic oscillations on the solar surface, the photosphere, powered by p-mode oscillations.

Liu et al. (2021) developed a new granule segmenting method allowing to detect two critical sizes of granules, 265 and 1420 km. The granules with sizes above 1420 km follow Gaussian distribution, and demonstrate flat in flatness function, which shows that they are non-intermittent and thus are dominated by convective motions. Small granules with sizes between 265 and 1420 km are fitted by a combination of power-law function and Gauss function, and exhibit nonlinearity in flatness function, which reveals that they are in the mixing motions of convection and turbulence. Mini granules with sizes below 265 km follow the power-law distribution and demonstrate linearity in flatness function, indicating that they are intermittent and strongly turbulent. These results suggest that a cascade process occurs: large granules break down due to convective instability, which transports energy into small ones; then turbulence is induced and grows, which competes with convection and further causes the small granules to continuously split. Eventually, the motions in even smaller scales enter in a turbulence-dominated regime.

Gao et al. (2021) analyzed four isolated BPs that showed area and average intensity oscillations lasting for several cycles in an in-phase fashion. The oscillation periods range from 100 to 200 seconds. We interpreted the phase relation as a signature of sausage waves, particularly slow waves, after discussing sausage-wave theory and the opacity effect.

Wang et al. (2022) analyzed high-spatial-resolution magnetograms and H $\alpha$ off-band ( $\pm 0.8 \text{ \AA}$ ) GST images to study magnetic properties of small-scale ejections near the boundary of a CH. They focused on the magnetic structure and evolution by tracking magnetic features with the Southwest Automatic Magnetic Identification Suite (SWAMIS). The magnetic field at the studied CH boundary was found to be dominated by negative polarity with flux cancellations at the edges of the negative unipolar cluster. In a total of 1250 SWAMIS-detected magnetic cancellation events, 39% were located inside the CH with an average flux cancellation rate of  $2.0 \times 10^{18} \text{ MxMm}^{-2}\text{hr}^{-1}$ , and 49% were located outside the CH with an average flux cancellation rate of  $8.8 \times 10^{17} \text{ MxMm}^{-2}\text{hr}^{-1}$ . Authors estimated that the magnetic energy released due to flux cancellation inside the CH is six times more than that outside the CH. Flux cancellation accounts for about 9.5% of the total disappearance of magnetic flux. Other forms of its disappearance are mainly due to fragmentation of unipolar clusters or merging with elements of the same polarity. We also observed a number of significant small-scale ejections associated with magnetic cancellations at the CH boundary that have corresponding EUV brightenings.

Liu et al. (2022b) found a critical size that divides the granules in motions into two regimes: convection and turbulence. The length scales of granules with sizes

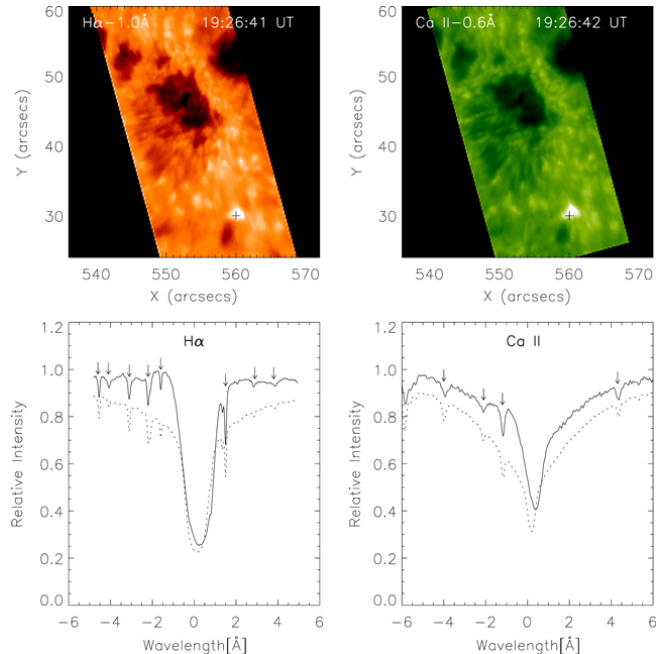


**Figure 5.** FISS raster images and H $\alpha$  and Ca II 8542  $\text{\AA}$  spectral profiles. The images were obtained at the H $\alpha$  ( $-1.0 \text{ \AA}$ ) and Ca II ( $-0.6 \text{ \AA}$ ) wings. In the lower plots the solid lines are spectral profiles at the brightening site ( $560''$ ,  $30''$ ), while the dotted lines are spatially averaged profiles. The vertical arrows denote telluric lines. Adopted from Kim et al. (2015).

larger than 600 km follow Gauss function and demonstrate "flat" in flatness, which reveal that these granules are dominated by convection. Those with sizes smaller than 600 km follow power-law function and behave power-law tendency in flatness, which indicate that the small granules are dominated by turbulence.

## 2. ELLERMAN BOMBS

Ellerman bombs (EBs) are short-lived energy release events that appear as a bright feature in the far wings of the Balmer lines, especially the H $\alpha$  line, while the core of these lines usually remains unchanged, suggesting that these events occur in the lower chromosphere (Fig. 5). Their typical size is  $1''$  and their lifetime is a few minutes. It is widely accepted that magnetic reconnection in the low chromosphere is responsible for EBs. Observational studies showed that EBs are often detected in association with a bipolar emerging flux (EF) or moving magnetic features (MMFs). Recent studies also showed that EBs may be accompanied by elongated granule-like features (EGFs) displaying transverse motions.

Yang et al. (2016) showed a clear connection among emerging magnetic flux, photospheric features, and EBs (Figure 6). EBs appear to result from magnetic reconnection forced by an EF or MMFs. Some of these events were accompanied by EGFs that showed transverse motions prior to the EBs with an average speed of about  $3.8 \text{ km s}^{-1}$  (see also Yang et al. 2013). Each EGF con-

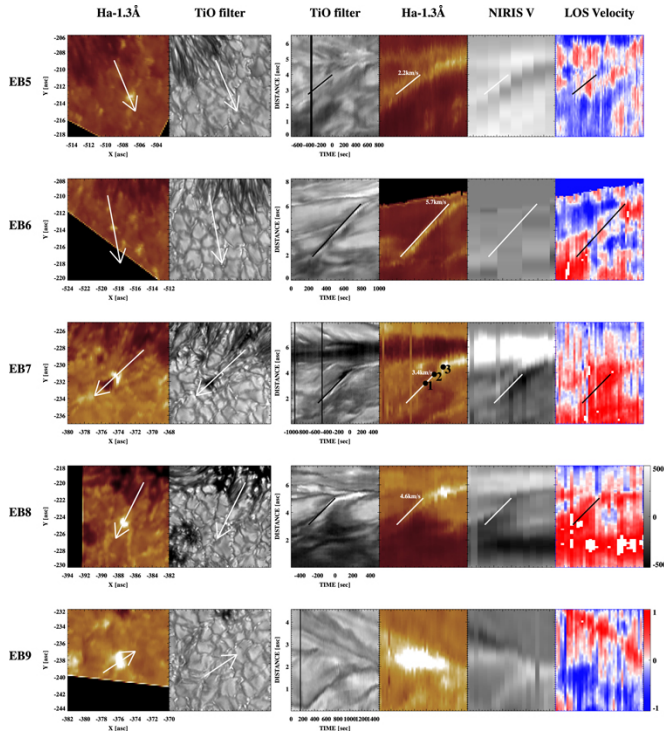


**Figure 6.** Raster images of the five EBs shown during their intensity peak at  $H\alpha$ -1.3  $\text{\AA}$  raster images (two left columns), and the d-t plots derived from TiO,  $H\alpha$ -1.3  $\text{\AA}$ , NIRIS longitudinal magnetic field, and LOS velocity data (four right columns). Adopted from Yang et al. (2016)

sisted of a sub-arcsecond bright core encircled by a dark lane around its moving front. The bright core appeared in broadband TiO images, and in far wings of the  $H\alpha$  and Ca II 8542  $\text{\AA}$  lines. Bi-directional expanding motion of the EGFs was identified in TiO data for four EBs, and they were found to be accompanied by an EF. Sometimes EGFs may develop at the edge of a penumbra and travel in the sunspot’s radial direction in which case they may be observed as MMF.

Kim et al. (2015) presented the first simultaneous observations of IRIS “hot explosions” using GST and IRIS instruments. An elongated granule seen in GST TiO data is clear evidence that emergence of a positive flux may trigger a hot explosion event, which was also observed as an EB in the wings of the  $H\alpha$  line although its intensity was weak and the vertical extent of the brightening seems to be relatively high compared to the typical EBs.

Hong et al. (2014) studied FISS spectra of four typical EBs observed in an AR using a two cloud model approach. The lower cloud was accountable for the source function, that suggested a temperature increase of 400-1000 K in EBs relative to the QS thus confirming that local heating occurs in the lower atmosphere. However,

the derived velocities differed from the bisector method velocities.

Hong et al. (2017a) performed a spectral analysis of EBs using FISS and IRIS data that showed clear evidence of heating in the lower atmosphere, indicated by the wing enhancement in  $H\alpha$ , Ca II 8542  $\text{\AA}$ , and Mg II triplet lines. However, authors did not find any signatures of heating in IRIS hotter lines (C II and Si IV). Two-cloud model showed a temperature enhancement of 2300 K, which is among the highest of previous modeling results, albeit still insufficient to produce IB signatures at ultraviolet wavelengths.

Li et al. (2015) performed semi-empirical atmospheric modeling and found that heating may occur near the temperature minimum region with a temperature increase of 2700-3000 K, which is surprisingly higher than previously thought. The radiative and kinetic energies are estimated to be as high as  $5 \times 10^{25} - 3 \times 10^{26}$  erg despite the small size of these EBs, which appeared in a region of mixed polarities. Nonlinear force-free field extrapolations revealed that three EBs were associated with a series of field lines with bald patches, which strongly implies that these EBs should be produced by magnetic reconnection in the solar lower atmosphere.

Fang et al. (2017) Used non-LTE semi-empirical modeling of line profiles, continuum emission and radiative losses of EBs with different temperature increases, and compare them with observations. Authors found that when the modeled EB temperature exceeds 10 000 K near the temperature minimum region, then the resulting  $H\alpha$  and Ca II 8542  $\text{\AA}$  line profiles and the continuum emission are much stronger than observed. This is in disagreement with recent reports that the temperature of EBs could be in excess of 10 000 K. Moreover, due to the high radiative losses, such high temperature can be sustained only for a very short interval, which is not compatible with observations.

Seo et al. (2019) modeled EB heating by a local temperature increase above the quiet-Sun temperature to find that FISS  $H\alpha$  and Ca II 8542  $\text{\AA}$  intensity profiles cannot be simultaneously reproduced by a single temperature bump model as long as the hot region is thicker than 100 km. Simultaneous reproduction of both lines is possible when the EB temperature enhancement is confined to a <20 km the photosphere, where the  $H\alpha$  wing response function is high and that of the Ca II 8542  $\text{\AA}$  is not. They also found that an EB at the time of its weakest appearance is located at lower heights,  $\sim 50$  km, and it moves upward to  $\sim 120$  km as it intensifies.

Chen et al. (2019) investigated the spatial and temporal relationship between flame-like EBs and UV bursts. In total, 161 EBs have been identified in GST data and about 20 of them revealed signatures of IRIS UV bursts. These UV bursts have a tendency to appear on top of their associated flame-like EBs and their intensity variations match well. The data suggest that some of UV

bursts and EBs are likely to form at different heights during a common reconnection process.

Wang et al. (2020a) analyzed vector magnetic fields, continuum images, and  $H\alpha$  data for NOAA AR 12665 in order to understand signatures of small-scale flux emergence, as well as their atmospheric response. Authors report that while in general flux emergence is associated with darkening of granular boundaries, only flux sheet emergence may elongate granules along the direction of emergence. The total emerged vertical flux is on the order of  $10^{18}$  Mx. The magnitudes of the vertical and horizontal emerging fields are comparable in the case of flux sheet emergence, while the former is stronger in a flux loop type of emergence.  $H\alpha$  observations reveal transient brightenings in the wings in the events of magnetic loop emergence, which are most probably the signatures of Ellerman bombs.

### 3. SMALL-SCALE RECONNECTION AND CHROMOSPHERIC FLOWS

Cao et al. (2010) found that the dark upflows propagating along the filament channel are strongly associated with intensity oscillations near the filament footpoints. The upflows start at the same time as the peak in the oscillations, illustrating that the upflow velocities are well correlated with them. Also, the intensity of one of the seven upflows showed periodic variations with the period gradually varying from 10 to 5 minutes.

Chae et al. (2010) studied magnetic reconnection in a QS area by tracking the morphology and dynamics of plasma visible in the  $H\alpha$  line associated with a canceling magnetic feature (CMF). Reconnection involved four magnetic domains and resulted in eruption of a small plasma cloud with a plane-of-sky speed of  $10 \text{ km s}^{-1}$ , a brightening, and tiny shrinking bright loops. Authors argued that this reconnection occurred in the chromosphere and it may be responsible for CMFs.

Yurchyshyn et al. (2010) reported that even very small dipoles (elements separated by about  $0''.5$  or less) may reach the chromosphere and trigger non-negligible chromospheric activity. Apparent collision and disappearance of two opposite polarity elements may not necessarily indicate their cancellation (i.e., reconnection, emergence of a “U” tube, or submergence of  $\Omega$  loops). In this case, the magnetic dipole disappeared by reconnecting with overlying large-scale inclined plage fields.

Goode et al. (2010); Yurchyshyn et al. (2011) observed intergranular jets associated with granular fragmentation, in particular, with the formation and evolution of a bright granular lane (BGL) within individual granules. Signatures of a BGL may reach the lower chromosphere and can be detected in off-band  $H\alpha$  images. Simulations also indicated that vortex tubes may be associated with small-scale magnetic fields. Authors speculate that the intergranular jets may result from the interaction between the turbulent small-scale fields associated with

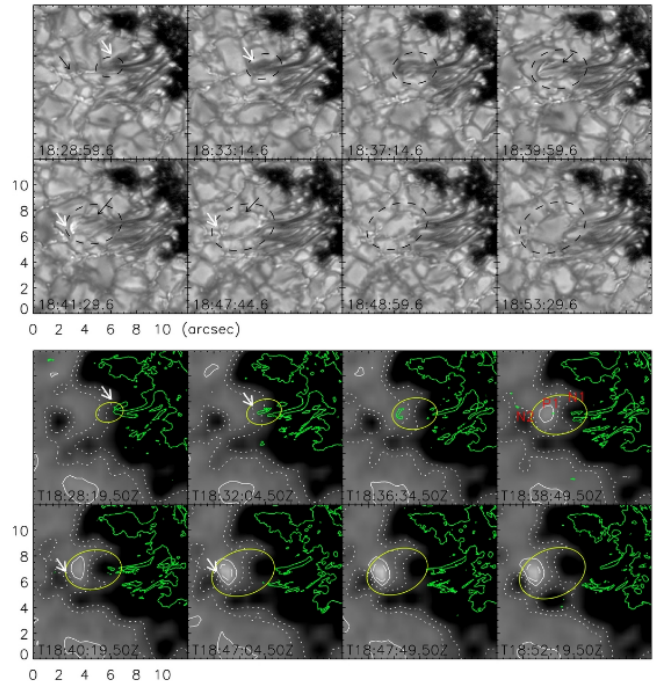


**Figure 7.** Top: time series of TiO observations taken on 2010 September 27. Black dashed ovals indicate the GLF of interest, white arrows the farther footpoint of the GLF from the pore, and black arrows the thread structure of the GLF. Bottom: line-of-sight SDO/HMI magnetograms (background) spatially and temporally co-aligned with TiO data (green contours). White contours indicate the magnetic flux, dotted curves correspond to the magnetic flux of (-50, -100 G), solid curve to (0 G), and the dashed curve to (+50 G). The same white arrows and ovals shown in the top panel are also marked in the magnetograms. P1 and N1 denote positive and negative magnetic flux at footpoints of the GLF, and N2 denotes a pre-existing negative flux. Adopted from Lim et al. (2011)

the vortex tube and the larger-scale fields existing in the intergranular lanes.

Lim et al. (2011) studied flux emergence events on a sub-granular scale and found several elongated granule-like features (GLFs) stretching from the penumbral filaments of a sunspot at a relatively high speed of over  $4 \text{ km s}^{-1}$  (Figure 7). The size of a GLF was approximately  $0''.5$  wide and  $3''$  long. These GLFs are photospheric manifestations of small-scale flux emergence, and their disappearance is related to magnetic cancellation.

Yurchyshyn et al. (2013) used  $H\alpha$ -0.1 nm and magnetic field (at  $1.56\mu$ ) data to suggest that the occurrence of rapid blue-shifted excursions (RBEs) is generally correlated with the appearance of new, mixed, or unipolar fields in close proximity to network fields. RBEs show a tendency to occur at the interface between large-scale

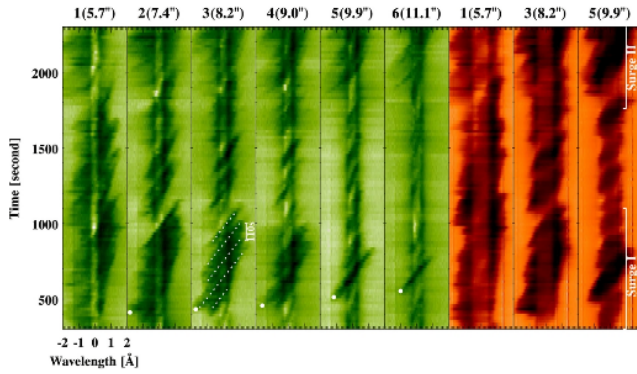


**Figure 8.** Wavelength–time plots in Ca II 8542 Å (leftmost six plots) and H $\alpha$  (rightmost three plots) lines at six spatial positions marked by the white dots in Figure 1. The numbers in parentheses represent the distance from the brightening positions in the SDO/AIA 1600 Å images. Two big surges appeared during the time interval of 300–1100 s and 1760–3542 s. The white dots are the positions where the largest amplitude shock features were first shown in each plot. Adopted from Lim et al. (2011).

fields and small-scale dynamic magnetic loops and thus are likely to be associated with the existence of a magnetic canopy. Detection of kinked and/or inverse “Y”-shaped RBEs further confirm this conclusion.

Chae et al. (2013) confirmed that the bisector of the spatially averaged Ca II line profile has an inverse C-shape with a significant peak red-shift of  $+1.8 \text{ km s}^{-1}$ . In contrast, the bisector of the spatially averaged H $\alpha$  line profile has a C-shape with a small peak blue-shift of  $-0.5 \text{ km s}^{-1}$ . In both lines, the bisectors of bright network points are significantly red-shifted not only at the line centers, but also at the wings. The Ca II Doppler shifts are found to be correlated with the H $\alpha$  ones with the strongest correlation occurring in the internetwork region. Moreover, they found that the Doppler shifts in the two lines are essentially in phase.

Yang et al. (2014) argued that a surge may consist of multiple shock features (Figure 8). They observed overlapping shocks with the time interval of 110 s, which is much shorter than the duration of each shock feature (300–400 s). These multiple shock waves in charge of the surge could have been generated by the magnetic reconnection that occurred in the low atmosphere in association with the flux cancellation.

Vargas Domínguez et al. (2014) reported that the orientation of the emerging magnetic field lines formed an angle of  $\sim 45^\circ$  with the overlying ambient field and their interaction caused high-temperature emission and plasma jets. The localized heating is detected before and after the first signs of the surge/jet ejection 9.

Ahn et al. (2014) observed plasma material falling along the loop from a coronal height and into the umbra of a sunspot, accompanied by C2 and C7 flares

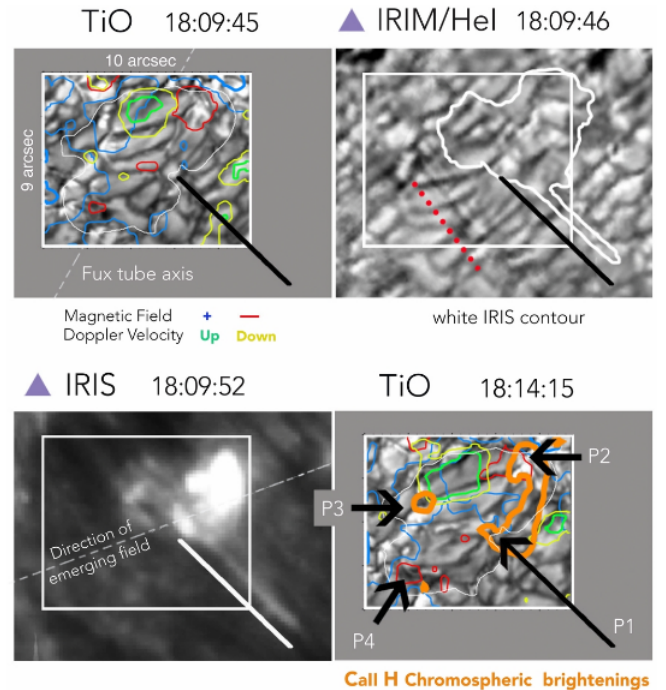


**Figure 9.** Sequence of selected GST (TiO and He I) and IRIS images displaying the evolution of the region where granular alignments are detected. Colored contours are LOS-magnetic field ( $\pm 40 \text{ G}$ ) and Doppler velocities ( $\pm 160 \text{ m s}^{-1}$ ). He I 1083 nm is shown at the time the jet is visible in IRIS 133 nm (right). The IRIS contour is overplotted in white in the He I frame. In the right frame, arrows indicate the location of points of interest (P1, P2, P3, and P4). Inclined solid lines are shown as references compared with IRIS image where the jet is observed. The axis of the emerging flux tube and the direction of the emerging magnetic field lines are denoted by inclined dashed lines in the first and third frames, respectively. The direction of the ambient field can be inferred from the He I 1083 nm image (see the dotted red line). Adopted from Vargas Domínguez et al. (2014).

near the loop. The temperature of the downflows was in the range of  $1 - 3.3^4 \text{ K}$ , increasing toward the umbra. There seemed to be a temporal correlation between the amount of downflow material and the observed C-class flares. The flows observed on-disk in H $\alpha$  and Ca ii 8542Å appeared as fragmented, fuzzy condensed material falling from the coronal heights when seen off-limb with STEREO/EUVI at 304Å. Based on these observations, authors proposed that these flows were an on-disk signature of coronal rain.

Vargas Dominguez et al. (2014) observed emergence of a small-scale magnetic-flux rope in the photosphere and the response of the solar atmosphere as emerged fields interacted with the pre-existing overlying fields. The reconnection process produced jets, emissions and high-temperature points in the chromosphere and corona.

Song et al. (2015) observed transient brightening of a coronal loop and an associated fine-scale photospheric magnetic discontinuity that represents a narrow lane of intense horizontal magnetic field representing. Variations of these horizontal fields suggest an increase of the magnetic non-potentiality at the loop footpoint and then sudden release of magnetic energy via magnetic reconnection, support the nanoflare theory that coronal heating.

Zeng et al. (2016) observed a small-scale chromospheric jet with bi-directional flows using the 1083 nm line, which may suggest that the jet was produced via magnetic reconnection in the upper chromosphere.

Li et al. (2016) observed a fan-shaped surge consisting of many 100 km wide threads ejected along large scale magnetic field lines. The associated H $\alpha$  brightening at the root of the surge indicated on low-atmosphere interchange magnetic reconnection confirming the for the fan-shaped surges reconnection model by Jiang et al.

Hong et al. (2017b) found that enhanced absorption in the 1083 nm line is spatially correlated with the enhanced average UV/EUV emission observed at 13.1, 17.1, 30.4 and 160 nm, while the high temperature emission observed at 9.4, 19.3, 21.1 and 33.5 nm lines does not show such tendency. The results provide further observational evidence that energy for heating the upper solar atmosphere comes from the intergranular lane area where the magnetic field is constantly brought in by convection motions.

Gopalan Priya et al. (2018) found that in many cases dynamic fibrils follow a nearly perfect parabolic path with the average maximum velocity around 15 km s<sup>-1</sup> and the mean deceleration of 100 ms<sup>-2</sup>. The observed deceleration appears to be a fraction of that caused by the gravity of the Sun and is not compatible with the path of a ballistic motion due to the gravity of the Sun. They also report a positive correlation between the deceleration and the maximum velocity, which is consistent with earlier simulations of upwardly propagating magneto-acoustic shock waves.

Şahin et al. (2019) presented two loop brightening episodes that were associated with magnetic flux emergence and cancellation events. The observed activity was driven by magnetic reconnection between small-scale emerging dipoles and large-scale pre-existing fields (Figure 10), suggesting that the reconnection occurred in the lower chromosphere at the edge of an extended plage region, where the loops were rooted. This study also indicates that at least some of the bright loops seen in SDO/AIA images rooted in sunspot the umbra may be heated due to magnetic activity taking place at the remote (non-sunspot) footpoint.

Cho et al. (2020) analyzed the spatiotemporal variation of the electron number density of plume structure in coronal holes above the limb for a given temperature, and find that the density perturbations accelerate with supersonic speeds in the distance range from 1.02 to

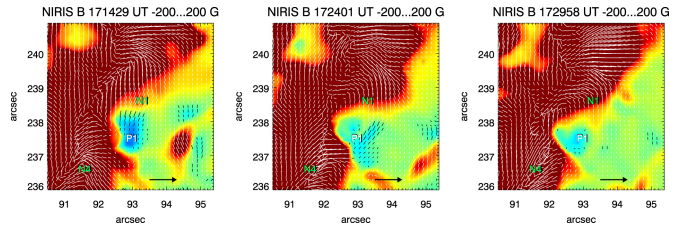


**Figure 10.** Evolution of the magnetic environment at the sunspot footpoint of the loop. The black arrow represents 2000 G transverse fields. The LOS fields (background) are scaled between -200 G (red) and 200 G (blue). “N1”, “P1”, and “N4” mark positions of the magnetic elements under discussion. The extended AIA 17.1 nm sunspot loop footpoint occupied space between N1 and N4. Adopted from Şahin et al. (2019).

1.23 solar radii. They interpreted them as slow magnetoacoustic waves propagating at about the sound speed with accelerating subsonic flows. The evolution of the nascent solar wind in plumes at the low corona is quantified for the first time from imaging observations. Based on the interpretation, propagating density perturbations present in plumes could be used as a seismological probe of the gradually accelerating solar wind.

Cho et al. (2019b) observed a propagating kink wave that was possibly excited by the repetitive spontaneous magnetic reconnection. An oscillating H $\alpha$  surge in a polar CH was detected changing its shape from a “C” to an inverse “C” configuration after a cusp was formed at the base of the surge. The plasma waves moving upward above the cusp and downward below it. The upflows showed right hand rotational motions with the rotation rate decreasing with height. The surge exhibited 2 min transverse oscillation near the cusp region and the phase of oscillations changed above the cusp, giving a vertical phase speed about 86 km s<sup>-1</sup>.

Yang et al. (2019b) performed detailed analysis of high-resolution spectroscopic He I 1083 nm and H $\alpha$  data acquired for a set of AR loops with counter-streaming motions along different strands. Based on wavelet analysis authors speculated that the counter-streaming motions in short loops could be powered by the  $p$ -mode leakage. However in long AR loops the counter streaming flows were accompanied with simultaneous weak EUV brightenings suggesting that the flow were likely driven by heating fueled by reconnection at loop footpoints.

Samanta et al. (2019) observed spicules emerging within minutes of the appearance of opposite-polarity magnetic flux around dominant-polarity magnetic field concentrations, while SDO data showed subsequent heating of the adjacent corona. The dynamic interaction of magnetic fields (likely due to magnetic reconnection) in the partially ionized lower solar atmosphere

appears to generate these spicules and heat the upper solar atmosphere.

Yurchyshyn et al. (2020a) presented evidence of very rapid morphological changes on timescales of the order of 1 s. Unlike typical reconnection jets, RBEs very frequently appear in situ without any clear evidence of H $\alpha$  material being injected from below. Their evolution includes inverted “Y”, “V”, “N”, and parallel splitting (doubling) patterns as well as sudden formation of a diffuse region followed by branching. We also find that the same feature may undergo several splitting episodes within about a 1 minute time interval.

Sterling et al. (2020) argued that morphologically, bursts of spicules, referred to as “enhanced spicular activities” by Samanta et al., appear as scaled-down versions of the jet’s chromospheric component. For two events they found candidates for corresponding erupting microfilaments. They conclude that erupting microfilaments might drive the enhanced spicular activities.

Abbasvand et al. (2020) researched the role of acoustic and magneto-acoustic waves in heating the solar chromosphere and found that in the middle chromosphere ( $h = 1000\text{-}1400$  km), the radiative losses can be fully balanced by the deposited acoustic energy flux in a quiet-Sun region. In the upper chromosphere ( $h > 1400$  km), the deposited acoustic flux is small compared to the radiative losses in quiet as well as in plage regions. The crucial parameter determining the amount of deposited acoustic flux is the gas density at a given height. The study concluded that the acoustic energy flux is efficiently deposited in the middle chromosphere, where the density of gas is sufficiently high. About 90% of the available acoustic energy flux in the quiet-Sun region is deposited in these layers, and thus it is a major contributor to the radiative losses of the middle chromosphere. In the upper chromosphere, the deposited acoustic flux is too low, so that other heating mechanisms have to act to balance the radiative cooling.

Wang et al. (2021) reported a detailed analysis of a small-scale chromospheric jet with high-resolution He I 10830 Å and TiO 7057 Å images. The data revealed the finest (100 km) dark threads inside the jet that were rooted in the intergranular lanes. Authors proposed that the jet might be initiated by magnetic reconnection in a U-shaped loop configuration. The feature may be used to explain the recurrent behavior of the jet, since the new U-shaped loop can be driven to reconnect again.

Hashim et al. (2021) observed temporal correlation between extreme-ultraviolet (EUV) emission and magneto-acoustic oscillations in an EUV moss region, which is the footpoint region only connected by magnetic loops with million-degree plasma. They reported the following: 1) repeated injections of chromospheric material appearing as 10830 Å absorption are squirted out from intergranular lanes with a period of about 5 minutes; 2) EUV emission is found to be periodically modulated with similar periods of about 5 minutes; 3) around the injection

area where 10830 Å absorption is enhanced, both EUV emissions and magnetic fields are remarkably stronger; and 4) EUV emission peaks are found to be in sync with oscillatory peaks of the stronger magnetic field in the region.

Madjarska et al. (2021) studied the chromospheric counterpart of small-scale coronal loops constituting a coronal bright point (CBP) and its response to a photospheric magnetic-flux increase accompanied by co-temporal CBP heating. They found that the counterpart of the CBP, as seen at chromospheric temperatures, is composed of a bundle of dark elongated features, which constitute an integral part of the CBP loop magnetic structure. An increase in the photospheric magnetic flux due to flux emergence is accompanied by a rise of the coronal emission of the CBP loops, that is a heating episode. They also observed enhanced chromospheric activity associated with the occurrence of new HJs and mottles. While the coronal emission and magnetic flux increases appear to be co-temporal, the response of the HJ counterpart of the CBP occurs with a small delay of less than 3 min, suggesting that the heating may have occurred at coronal heights.

Hong et al. (2022) described properties of four granule-sized He I 10830 Å microeruptions occurring at PILs with their roots in intergranular lanes. Two of the microeruptions were repetitive microjets, lasting about 50 and 27 minutes respectively, while the other two events were singular, lasting about 5 minutes. The recurrence was quasiperiodic with a period of  $\sim 5$  minutes. Authors note that in the case of the long duration microjets, granules with the concentration of a positive magnetic field persistently transport the magnetic field to the PILs, canceling the opposite magnetic flux and making the base of the two microjets and the underlying granules migrate with the speed of 0.25 and 1.0 km s $^{-1}$ . The observations support the scenario of magnetic reconnection for the quasiperiodic microjets and further show that the reconnection continuously generates multitemperature components, especially the cool component with chromospheric temperature. In addition, the ongoing reconnection is modulated by p-mode oscillations inside the Sun.

Zhao et al. (2022) studied a convection-driven recurrent fan-like jets and reported evidence of reconnection between the photosphere and chromosphere corresponding to the intergranular lanes.

Lee et al. (2022) studied properties of spicule-like events in the chromospheric network near the coronal hole boundary. Intervals between adjacent spicules located along the chromospheric network are found in the range of 0.4-1.5 Mm ( $0^\circ.03\text{-}0^\circ.12$ ) tending to be smaller than the medium scale of switchbacks (SBs). Interdistances between all pairs of the flux tubes are also counted and they appear in a single peak distribution around 0.7 Mm ( $0^\circ.06$ ) unlike the waiting-time distribution of SBs in a scale-free single power-law form.

The length-to-diameter ratio of the dense section of flux tubes is as high as 6-40, similar to the aspect ratio of SBs. The number of spicules along a network can be as high as 40-100, consistent with numerous SBs within a patch. With these numbers, it is argued that the medium scale of SBs can be understood as an equilibrium distance resulting from a random walk within each diverging magnetic field funnel connected to the chromospheric networks.

#### 4. STRUCTURE OF SUNSPOTS AND PORES

The sunspot umbra is filled with umbral dots (UDs) which are small bright patches seen embedded into the overall dark background. The UD has various size and often forms clusters, contributing to umbral non-uniformity. It is thought that UD is field-free plasma structure which forms when heated plasma beneath the sunspot is pushed upward into weaker field structures, squeezing in between gaps and openings thus making its way to the surface. The weaker the fields are associated with larger UD and brighter umbra. Kilcik et al. (2012) performed statistical studies of UD living longer than 150 s. Authors reported that UD is not circular in shape and that the diameter of only bright UD is proportional to their intensity, while their velocities are inversely related to the lifetime. Nearly all photospheric UD can be identified in the low chromospheric images, although some small closely spaced UD appear in the low chromosphere as a single unresolved structure. Comparison to the 3D MHD simulations showed that both types of UD display, on average, very similar statistical characteristics. However, the average number of observed UD per unit area is smaller than that of the model UD, and the diameter of model UD is slightly larger than that of observed ones, which indicates that the magnetic fields in the observed umbra are stronger than those in the model used.

Kilcik et al. (2020) analyzed average position distributions, location dependencies, and general properties of the detected total 2892 and reported that i) the brightest, largest, fastest and most elliptic UD tend to be located at the umbra-penumbra boundary while their lifetime does not display any meaningful location dependency; ii) average dynamic velocity of all detected UD is about twice (0.76 km/s) of the previously reported average values; iii) obtained trajectories from the longest-lived 354 UD show that they have generally inward motion; iv) chosen 10 long-lived UD generally have similar periodic behavior showing 8.5 - 32, 3.5 - 4.1, 1.5 - 1.9, and 1.1 - 1.3 minutes periodicities; v) detected UD have an elliptical shape with the averaged eccentricity of 0.29, with a 0.11 standard deviation; and vi) larger UD tend to be more elliptic and more dynamic.

The chromosphere above the photospheric umbra also hosts a plethora of structures. VIS off-band  $H\alpha$  images show the presence of chromospheric UD, which are generally a bit larger than the photospheric UD. At the

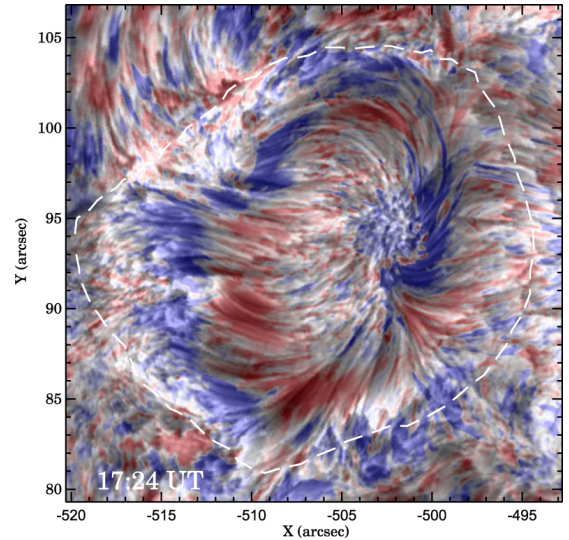


**Figure 11.** Composite image of  $H\alpha$  (grayscale) with the pseudo-Dopplergram (blue and red). The pseudo-Dopplergram is constructed by subtracting the red wing ( $H\alpha+0.6 \text{ \AA}$ ) from the blue wing images ( $H\alpha-0.6 \text{ \AA}$ ), with blue and red representing blueshifts and redshifts, respectively. Adopted from Jing et al. (2019).

$H\alpha$  line center the umbra appears to be filled with fine sub-arcsecond structures which Yurchyshyn et al. (2014) called umbral spikes. They are cool, cone-shaped, jet-like structures with a typical height of 0.5-1.0 Mm and the base width of about 0.1 Mm. Their lifetime ranges from 2 to 3 minutes and they tend to re-appear at the same location. The spikes are not associated with photospheric UD and they instead tend to occur above the darkest parts of the umbra where magnetic fields are strongest. The spikes exhibit up and down oscillatory motions and their spectral evolution suggests that they might be driven by upward propagating shocks generated by photospheric oscillations. It is worth noting that triggering of the running penumbral waves seems to occur during the interval when the spikes reach their maximum height.

One of the sunspot mysteries is the existence of the sunspot penumbra, which is a photospheric structure consisting of dark and bright filaments originating in the umbra and radially extending away from the sunspot center fully or partially encircling the umbra. The dark penumbral filaments are thought to be associated with horizontal magnetic, while the bright filaments host fields inclined at  $45\text{-}60^\circ$ . But how does the penumbra form? Lim et al. (2013) observed the formation of a partial penumbra for about 7 hr simultaneously using photospheric ( $\text{TiO}$ ,  $7057 \text{ \AA}$ ) and chromospheric ( $H\alpha-1.0 \text{ \AA}$ ) spectral lines. They found that the formation of the observed penumbra was closely associated with emergence of a new flux under the pre-existing chromospheric canopy fields. Authors suggested that a penum-

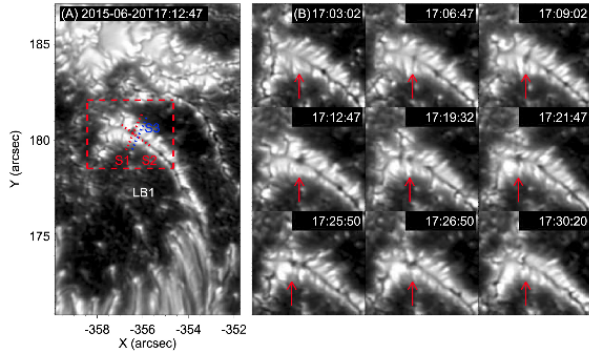


**Figure 12.** A) TiO image of NOAA AR 12371 taken at 17:12:47 UT on 2015 June 20. A narrow light bridge, LB1, is located in the center of the image. The dashed red box outlines the region shown in (B). The red dotted lines S1 and S2 mark two cuts for which we produce space-time diagrams shown in Figures 2(A) and (B), respectively. The blue dotted line S3 is perpendicular to the central dark lane. (B) Temporal evolution of a dark knot (indicated by the red arrows) observed between 17:03:02 UT and 17:30:20 UT. Adopted from Zhang et al. (2018).

bra forms when the emerging flux is constrained from continuing to emerge and is trapped at the photospheric level by the overlying chromospheric canopy fields. Li et al. (2018) studied development of a penumbra sector. Before the new penumbra sector formed, the developing sunspot already had two umbrae with some penumbral filaments. The penumbra sector gradually formed at the junction of two umbrae. First, the region where the penumbra sector formed appeared blue-shifted and this area, the mean transverse magnetic field strength, and the total magnetic flux of the umbra and penumbra sector all increased with time indicating magnetic field emergence. Next, after the penumbra sector appeared, the magnetic flux and the area of the penumbra sector increased while the umbra’s magnetic flux and area decreased. This study further confirmed that the penumbra formation resulted from a new emerging flux that was trapped in the photosphere. Moreover, authors argued that the penumbra sector further developed at the cost of the umbra.

The sunspot penumbra poses several challenging problems which are not yet fully solved. These include Evershed flows, formation of moving magnetic features (MMFs), as well as penumbral jets and brightenings. Deng et al. (2016) identified a total of 2692 penumbral bright dots (BDs) in IRIS 1400 Å slit-jaw images, which were associated more with downflows and darker fibrils in the chromosphere, and weakly associated with bright penumbral features in the photosphere. However, there is no consistent and convincing brightening in the chromosphere in response to the TR brightenings. Authors argue that penumbral BDs in the TR may be due to plasma falling from coronal heights along

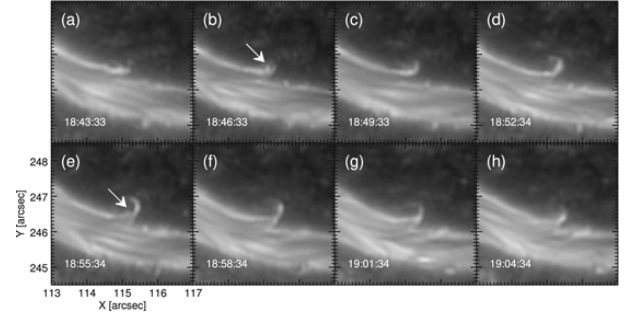


**Figure 13.** Formation of a filamentary vortex observed in the TiO broadband images. The white arrows represent secondary vortices when the vortex forms. Adopted from Yang et al. (2019a).

vertical and dense magnetic loops. The BDs may also be produced by small-scale impulsive magnetic reconnection taking place sufficiently high in the atmosphere that has no energy release in the chromosphere. Bai et al. (2016) detected a sub-arcsecond penumbral transient brightening, whose thermal energy was in the range of nano-flares, and it had signatures in the chromosphere, the transient region, and the corona. The width of the event was about 100 km ( $0''.14$ ), which is significantly less than that reported in previous studies. The small-scale energy released from the event has a multi-temperature component. Jing et al. (2019) observed a small pore with numerous fine-scale chromospheric super-penumbral fibrils (with an average cross-sectional width of  $0''.17pm0''.03$ ), along with associated transit and intermittent flows with apparent speeds of  $5\text{--}14\text{ km s}^{-1}$ . Analysis suggested that the observed flows along fibrils are not likely to be an oscillation/wave phenomenon. Instead, they may be a phenomenon similar to the inverse Evershed flow in the chromosphere (Figure 11).

Wang et al. (2018c) found that after a flare penumbral flows may be enhanced and reach unusually high speeds up to  $2\text{ km s}^{-1}$  along with extension of penumbral fibrils. They also found a gradual increase of shear flow velocity (up to  $\sim 0.9\text{ km s}^{-1}$ ) after the flare, accompanied by an increase of horizontal field and increase of magnetic inclination angle. MMFs is a dynamic magnetic structure consisting of two (sometimes one) opposite polarity magnetic elements, which “emerges” from extending penumbral fibrils and then rapidly moves across the sunspot moat. Lim et al. (2012) observed a bipolar MMF for the first time simultaneously in intensity images and magnetic field data. Results of full Stokes inversion revealed that the bipolar MMF had a U-shaped magnetic field configuration. The opposing view is that MMFs represent  $\Omega$  loops. Later, Li et al. (2019) performed a statistical study of physical properties of identified fine-scale MMFs such as size, lifetime, inclination, horizontal velocity, and flux.

Cho et al. (2013) found that the pores are filled with plasma which moves down slowly and are surrounded by a stronger downflow in the photosphere. In the lower chromosphere, they found that the plasma flows upward inside the pores while the plasma in small magnetic concentrations is always moving down. The upflow in the pores slows down with height and turns into downflow in the upper chromosphere while the downflow in the small magnetic concentrations gains its speed. The findings are in agreement with numerical studies that suggest that rapid cooling of the interior of pores drives a strong downflow, which collides with the dense lower layer below and rebounds into an upflow.

While many sunspots have one umbra fully surrounded by the penumbra, many sunspots exhibit a more complex with multiple umbrae (or umbral cores) separated by a much brighter areas called light bridges (LBs). A sunspot may have one or more LBs, which may have different width ( $0''.5$ - $2''.0$ ) and appearance. Wider LBs tend to resemble a QS photosphere with small well aligned granules and a dark central line running along the LB spine. Other LBs often have a filamentary structure as if penumbral filaments have intruded deep into the umbra. Zhang et al. (2018) observed knot-like dark structures within the central dark lane. Many dark knots migrate away from the penumbra along the LB (Figure 12). The size, intensity depression, and apparent speed are in the range of 80-200 km, 30%-50%, and  $0.3$ - $1.2$  km s<sup>-1</sup>, respectively. They also observed intergranular lanes crossing the LB and having the dynamic parameters similar to those of the dark knots. The intergranular lanes are associated with redshifts and located at two sides of each convection cell. The magnetic fields are stronger in intergranular lanes than in the central dark lane. These results suggest that these intergranular lanes are manifestations of convergent convective downflows in the light bridge. We also provide evidence that the dark knots observed in LB1 may have a similar origin. Yang et al. (2019a) observed successive occurrence of  $0''.5$  photospheric vortices (Figure 13) at the edge of a sunspot LB and the subsequent ejection of chromospheric surges that often exhibited a hollow cylindrical structure. It is likely that the vortices form under the Kelvin-Helmholtz instability. The surges may result from either the magnetic tension generated after magnetic reconnection or an acoustic impulse of a fast photospheric transverse flow. Otherwise, the surges could also be associated with Alfvénic waves, in which case their origin could be torsional magnetic fields generated in the process of the vortex formation.

Yang et al. (2019c) observed emergence of a new magnetic flux in a filamentary LB accompanied by brightness enhancement of a photospheric overturning convection cell (OCC) at the endpoints of the emerging magnetic structure. Changes in the orientation of the associated transverse fields, determined from the differential angle, suggest the emergence of a twisted mag-

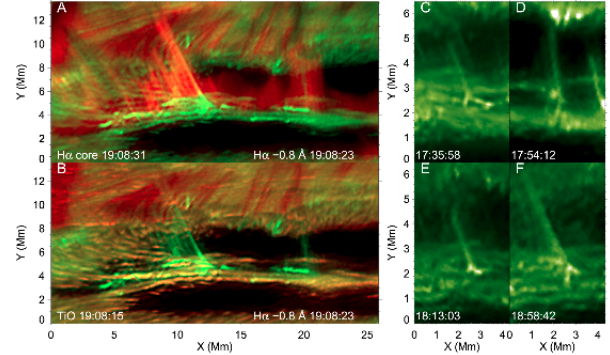


**Figure 14.** Examples of small-scale jets with an inverted Y-shape from the sunspot light bridges observed by GST on 2014 October 29. (A) Composite image of H $\alpha$  core (red) and wing at  $-0.8$  Å (green) at 19:08 UT. (B) Composite image of TiO (red) and H $\alpha$  wing at  $-0.8$  Å (green). (C–F) Images of H $\alpha$  wing at  $-0.8$  Å taken at four different times. An associated animation of panels A and B, covering from 17:30 to 19:42 UT, is available online. Adopted from Tian et al. (2018).

netic structure. A fan-shaped jet was observed to be spatially and temporally correlated with the endpoint of the OCC intruding into the LB. Bai et al. (2019) detected three-lobe Stokes V profiles and their inversion with the NICOLE code suggested that there may be opposite polarity magnetic fields in LBs. They found ribbon-like H $\alpha$ - $0.8$  Å brightenings propagating along the LBs, possibly indicating slipping reconnection, suggesting that the fan-shaped jets may be driven by magnetic reconnection and photospheric convective motions play an important role in triggering the magnetic reconnection.

Song et al. (2017b) observed arcsecond-scale chromospheric plasma ejections ( $1''.7$ ) inside a LB. Interestingly, the ejections are found to be a manifestation of upwardly propagating shock waves as evidenced by the saw-tooth patterns seen in the temporal-spectral plots of the Ca II 8542 Å and H $\alpha$  intensities. They also found a fine-scale photospheric feature ( $1''$ ) expanding with a speed of about  $2$  km s<sup>-1</sup> two minutes before the plasma ejections, which seems to be a manifestation of magnetic flux emergence. As a response to the plasma ejections, the corona displayed small-scale transient brightenings. They suggested that the shock waves can be excited by the local disturbance caused by magnetic reconnection between the emerging flux inside the LB and the adjacent umbral magnetic field. The disturbance generates slow-mode waves, which soon develop into shock waves, and manifest themselves as the arcsecond-scale plasma ejections. It also appears that the dissipation of mechanical energy in the shock waves can heat the local corona.

Tian et al. (2018) detect prevalent reconnection at LBs through frequently occurring fine-scale jets observed in

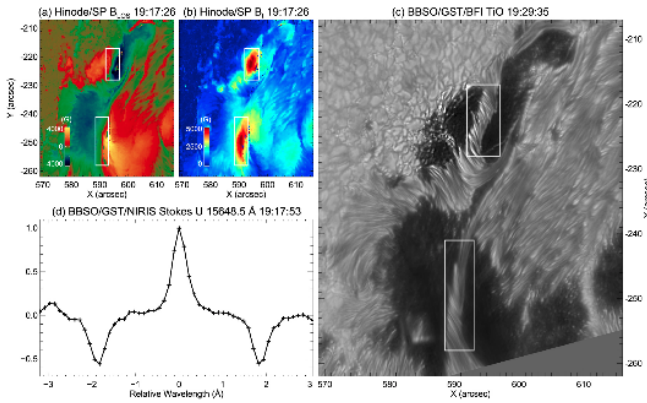


**Figure 15.** Unusual structures of AR 12673. (a) and (b) Hinode/SP LOS and transverse magnetic field strength. Note that in many pixels near the PIL, transverse fields are saturated at 5000 G. (c) BBSO/GST TiO image. The two white boxes in (a)-(c) mark the two strong transverse field areas at the PIL, where twisted photospheric LB structures of the  $\delta$  configuration are present. (d) NIRIS Stokes U profile of a selected strong transverse field pixel at the PIL within the northern box. The direct measurement of Zeeman splitting yields a field strength of 5570 G. Adopted from Wang et al. (2018b).

the  $H\alpha$  line wings. Many jets have an inverted Y-shape, shown by models to be typical of reconnection in a unipolar field environment (Figure 14). Simultaneous spectral imaging data from the Interface Region Imaging Spectrograph show that the reconnection drives bidirectional flows up to  $200 \text{ km s}^{-1}$ , and that the weakly ionized plasma is heated by at least an order of magnitude up to  $\sim 80,000 \text{ K}$ . Their observations also revealed that the surge-like activity previously reported above LBs may have two components: the ever-present short surges likely to be related to the upward leakage of magneto-acoustic waves from the photosphere, and the occasionally occurring long and fast surges that are obviously caused by the intermittent reconnection jets.

At times the magnetic fields emerging within LBs may be quite strong. Wang et al. (2018b) observed that an LB in a  $\delta$  configuration, may possess very strong and twisted magnetic fields (above 5500 G) as evidenced by twisted fibril structures observed in the photosphere (Figure 15). Lozitsky et al. (2018) studied Stokes parameters measured at about 70 various locations of the same sunspot and found that at in the umbra the magnitude of the magnetic field is in general greater, the umbral intensity is lower, and the maximum field there does not exceed 4 kG. However, in LBs the intensity of the spectral continuum is higher and the magnetic field strength there is in the range of 3.0-5.7 kG. The magnetic field inclination there suggests the dominance of horizontal and twisted fields.

Lim et al. (2020) performed magnetic field measurements and imaging spectroscopy of an LB with repetitive jetting activity. The authors detected magnetic flux emergence in the LB that is of opposite polarity to that of the sunspot. The new magnetic flux canceled with the pre-existing flux at a rate of  $5.6 \times 10^{18} \text{ Mx/hr}$ . Both the recurrent jet-like ejections and their base brightenings are initiated at the vicinity of the magnetic flux cancellation, suggesting that they may have resulted from slipping reconnection between the new flux emerging in the LB and the ambient sunspot field.

Lozitsky et al. (2022) studied very strong magnetic fields in the NOAA AR 12673, which was the most flare productive AR in solar cycle 24. Direct measurements of full Zeeman splitting of the Fe I 1564.85 nm line using all Stokes I, Q, U, and V profiles allowed them to obtain reliable estimates of the magnitude of magnetic fields independent of the filling factor and atmosphere models. Thus, the strongest fields up to 5.5 kG were found in an LB of a spot, while in the dark umbra magnetic fields did not exceed 4 kG. In the case of the LB, the magnitude of the magnetic field is not related to the underlying continuum intensity, while in the case of umbral fields authors observed a well-known anti-correlation between the continuum intensity and the field magnitude. A comparison of the depth of the Zeeman  $\pi$  and  $\sigma$  components showed that in the LB magnetic fields are, on average, more horizontal than those in the dark umbra.

Liu et al. (2022a) studied a small fan-shaped jet along a LB that developed within a few minutes, with diverging beams. At its base, a bright point was slipping along the LB and ultimately invaded the umbra of the sunspot. The multi-wavelength analysis suggested that the fan-shaped jet could result from magnetic reconnection across the highly diverging field low in the chromosphere, leading to an apparent slipping motion of the jet material along the LB. Authors, however, did not find any opposite magnetic polarity at the jet base, as would typically be expected in such a configuration.

## 5. SUNSPOT OSCILLATIONS

Andić et al. (2013) The movement of the footpoints of flux tubes in the photosphere indicated flux tube entanglement and magnetic reconnection as a possible cause of the observed brightening and waves propagating in the chromosphere. An upward propagating train of waves was observed at the site of the downflow event in  $H\alpha$ . There was no clear relationship between the photospheric waves and the Ca II and  $H\alpha$  events. Observations indicate that chromospheric waves that were previously thought to originate from the photosphere may be generated by some events in the chromosphere as well.

Maurya et al. (2013) Temporal-sequence analysis of FISS data showed enhanced high-frequency oscillations inside the sunspot umbra in both  $H\alpha$  and Ca II 854.2 nm lines. Their peak frequency gradually decreases outward

from the umbra. The oscillation power is found to be associated with magnetic field strength and inclination, with different relationships in different frequency bands.

Chae et al. (2014) reported observational finding that  $H\alpha$  fibrils in the super-penumbra of a sunspot are powered by sunspot oscillations. The patterns of outward propagation may be originating from inside the sunspot, propagate across the penumbra as running penumbral waves and then develop into the fibrils. The predominant period of these shock waves increases, often jumping with distance, from 3 minutes to 10 minutes. This short-to-long period transition seems to result from the selective suppression of shocks by the falling material of their preceding shocks. The authors proposed that the super-penumbral fibrils are driven by slow shock waves with long periods, which are produced by merging of shorter period shock waves propagating along the magnetic canopy.

Chae et al. (2015) provided observational evidence that shock merging does occur quite often in the chromosphere of sunspots. FISS  $H\alpha$  x-t plots show a number of alternating redshift and blueshift ridges (Figure 16) and The important finding is that two successive shock ridges often merge with each other. This finding can be theoretically explained by the merging of magneto-acoustic shock waves propagating with lower speeds of about  $10 \text{ km s}^{-1}$  and those propagating at higher speeds of about  $16\text{-}22 \text{ km s}^{-1}$ . The shock merging is an important nonlinear dynamical process of the solar chromosphere that can bridge the gap between higher-frequency chromospheric oscillations and lower-frequency dynamic phenomena such as fibrils.

Yurchyshyn et al. (2015a) reported that UFs appeared in the form of narrow bright lanes stretched along LBs and around clusters of UDs. The time series also suggested that UFs preferred to appear on the sunspot-center side of light bridges, which may indicate the existence of a compact sub-photospheric driver of sunspot oscillations. The power spectra analysis showed that the intensity of chromospheric and transition region oscillations significantly vary across the umbra and with height, suggesting that umbral non-uniformities and the structure of sunspot magnetic fields may play a role in wave propagation and heating of umbral loops (Figure 17). On the other hand, Şahin et al. (2019) observed bright umbra rooted UV loops that were heated due to magnetic activity taking place at the remote (non-sunspot) footpoint.

Cho et al. (2015) found that pore intensity displays three-minute oscillations and there is no phase difference between the intensity and the LOS velocity oscillations at a given wavelength. These results support the idea of a slow magneto-acoustic wave propagating along the magnetic field lines in the pores.

Su et al. (2016a) found that the running umbral waves with periods of 2.2-2.6 minutes underwent very fast damping before approaching umbral boundaries, while

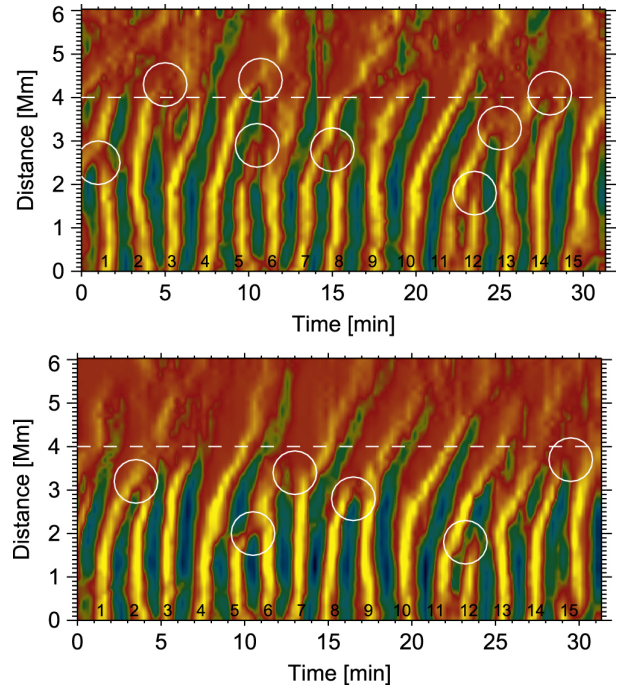


**Figure 16.** Time–distance maps of time derivatives of Doppler velocity along cut A (top) and cut B (bottom), respectively. The bright yellow refers to the region of rapid change from downward to upward velocity, and hence the highly compressed region that we identify with the shock front. Adopted from Chae et al. (2015).

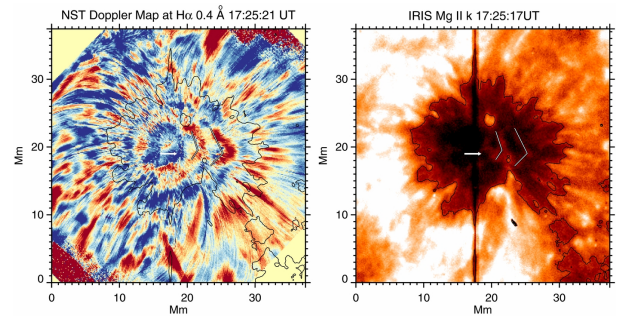


**Figure 17.** GST  $H\alpha$ -0.4Å Doppler map (left) and IRIS Mg II k slit-jaw image. The black contour outlines the Mg II k sunspot and is drawn at an arbitrary level. The white arrow points to a blueshifted feature in the  $H\alpha$  Doppler map that corresponds to the R1 UF lane. The two broken line segments mark two low contrast Mg II k UF fronts that are co-spatial with the two redshifted features in the  $H\alpha$  Doppler map. Adopted from Yurchyshyn et al. (2015a).

those with higher periods ( $>2.6$  minutes) could propagate outside umbrae. On two sides of each LB adjacent to umbrae, the cross-wavelet spectra displayed that the oscillations on them had a common significant power region with dominant frequencies of 2-6 minutes and phase differences of  $90^\circ$ . A counterstream of two running um-

bral waves in the 2-6 minute frequency range propagated toward the LBs, where they encountered each other and gave rise to constructive or even destructive interference on the LBs. In addition, the velocity and density perturbations on the LBs were found in opposite phases suggesting that the perturbations were caused by the downward propagating waves.

Su et al. (2016b) also reported that the apparent wavefronts of umbral waves may rotate both clockwise and anti-clockwise as well as form multi-armed spiral structures. Authors suggest that an one-armed spiral structure may be produced by the wave front reflecting at a LB, while the multi-armed spirals may be related to the twist of the magnetic field in the umbra. This indicates that these disturbances are slow magnetoacoustic waves in nature, and that they propagate upward along the inclined lines with fast radial expansions causing horizontal velocities of the running waves.

Kwak et al. (2016) reported three-minute oscillations in the solar chromosphere driven by a strong downflow event in a sunspot. The characteristics of the downflowing material are consistent with those of sunspot plume.

Zhao et al. (2016) applied a time-distance helioseismic analysis over a suite of multi-wavelength observations above a sunspot, we demonstrate that the helioseismic p-mode waves are able to channel up from the photosphere through the chromosphere and transition region into the corona, and that the magneto-acoustic waves observed in different atmospheric layers are a same wave originating from the photosphere but exhibiting differently under different physical conditions. They also showed that waves of different frequencies travel along different paths, which can be used to derive the physical properties of the atmosphere above sunspots.

Chae et al. (2017) found a local enhancement of the 3 minute oscillation power in the vicinity of a LB and numerous UDs (Figure 18). These 3 minute oscillations occurred independently of the 5 minute oscillations. The 3 minute oscillations were found to be consistent with the upwardly propagating slow magnetoacoustic waves in the photosphere with energy flux large enough to explain the chromospheric oscillations. Our results suggest that the 3 minute chromospheric oscillations in this sunspot may have been generated by magnetoconvection occurring in the LB and UDs.

Chae and Litvinenko (2017) presented a new analytical solution that describes a finite-amplitude wave of an arbitrary wavelength. The analytical results suggest that observations of three-minute oscillations in the solar chromosphere may reveal the basic nonlinear effect of oscillations with combination frequencies, superposed on the normal oscillations of the system. Authors also presented observational evidence of the second harmonic inferred from time variations of velocity determined from the Na I D2 and H $\alpha$  lines.

Song et al. (2017a) reported three-minute chromospheric oscillation above a sunspot triggered by a small-

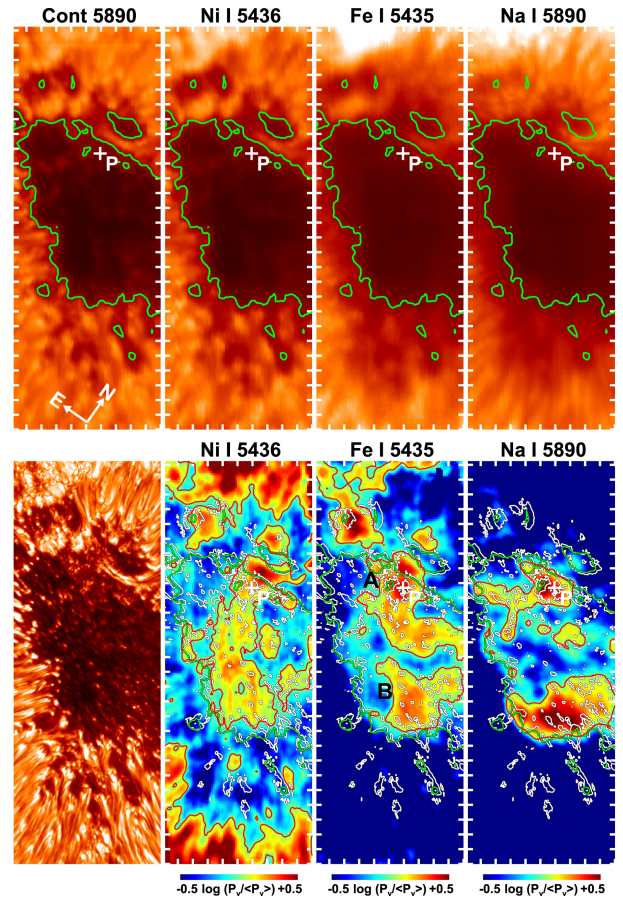


**Figure 18.** Top: intensity images constructed from a scan at the continuum and the cores of the three lines. The tick interval is 1000 km. The solar north and the solar east are indicated by the arrows. The FISS continuum contours (green curves) of 50% of the quiet region intensity are plotted to represent the umbra–penumbra boundary. The plus symbol marks the point P where the power and covariance spectra of velocity are examined in detail as an example (see Figure 4). Bottom: a map of the TiO broadband high-resolution image constructed at the same time as the above intensity maps, and power maps of one of the 3 minute velocity oscillations integrated over periods from 2 to 4 minutes and over 40 minutes in the three lines. A and B are two sub-regions of strong power. The TiO intensity contours (white curves) of 50% show the UDs in the umbra. The red contours indicate the average power level of the umbra. Adopted from Chae et al. (2017).

scale transient brightening in the LB composed of elementary bursts that may be a manifestation of fast repetitive magnetic reconnections. The initial period of the oscillations was about 2.3 minutes and then gradually increased to 3.0 minutes with time.

Priya et al. (2018) reported that 5 minute oscillation signals appear in the sunspot outside the umbral center, mostly with vertical magnetic field inclination  $>15^\circ$ .

The initial emergence of the 3 minute umbral oscillatory events was found to be closer to or at the umbral boundary. Nearly all umbral oscillatory events connect to the earlier occurring RPWs and also develop into new RPWs.

Kang et al. (2019) explored spiral wave patterns (SWPs) in 3 minute oscillations of sunspot umbrae using an analytical model that interprets the observed SWPs as the superposition of two different azimuthal modes of slow magnetoacoustic waves driven below the surface in an untwisted and non-rotating magnetic cylinder. The observed spiral structures are thus explained by the superposition of non-zero azimuthal modes driven 1600 km below the photosphere in the pore. The one-armed SWP is produced by the slow-body sausage ( $m = 0$ ) and kink ( $m = 1$ ) modes, and the two-armed SWP is formed by the slow-body sausage ( $m = 0$ ) and fluting ( $m = 2$ ) modes of the magnetic flux tube forming the pore.

Cho et al. (2019a) argued that magnetoconvection associated with UDs can drive 3 min umbral oscillations. They identified four oscillation centers with the power of the oscillations in these centers concentrated in the 3 minute band. These oscillation centers were located above UDs undergoing noticeable morphological and dynamical changes that may be regarded as an observable signature of small-scale magnetoconvection inside the umbrae.

Sych et al. (2020) obtained the spatial structure of oscillation sources as the footpoints of fine magnetic tubes, anchored in the sunspot umbra. Authors suggested that the observed spatial distribution of wave sources indicates the existence of a slow subphotospheric resonator with a vertical magnetic field in the umbra and a wave cutoff frequency due to inclination of the magnetic field line in the penumbra.

Yurchyshyn et al. (2020b) showed that UFs do not randomly originate over the umbra. Instead, they appear to be repeatedly triggered at locations with the lowest umbral intensity and the most powerful oscillations of  $H\alpha$ -0.04 nm intensity. The dominant location of prevalent UF origin is cospatial with the strongest fields in the umbra. The data confirms the idea that UFs may be driven by a subsurface source located near the axis of a flux rope, while the presence of several UFs trigger centers may indicate the complex structure of a sunspot umbra.

Cho and Chae (2020) inferred the depth of the internal sources driving three-minute umbral oscillations using Fe I 5435Å spectral data acquired by FISS. They identified five ripples and determined the propagation distance as a function of time in each ripple. From the model fitting to these data, we obtained the depth between 1000 and 2000 km. The finding may serve as an observational constraint to understanding the detailed processes of magnetoconvection and wave generation in sunspots.

Li et al. (2020) studied sunspot oscillations using CO 7-6 R67 and 3-2 R14 lines measured by the Cryogenic Infrared Spectrograph (CYRA), as well as the line profile of Mg II k line that was detected by the Interface Region Imaging Spectrograph (IRIS). They detected a 5-min periodicity in the umbra at the Doppler velocity range of the CO 7-6 R67 line that formed in the photosphere, while a periodicity of around 3 min is discovered at the Doppler velocities of CO 3-2 R14 and Mg II k lines that formed in the upper photosphere or the temperature minimum region and the chromosphere.

Chae et al. (2021) reported the first spectroscopic detection of Alfvénic waves around a sunspot at chromospheric heights. By analyzing the spectra of the H $\alpha$  line and Ca II 854.2 nm line, authors determined line-of-sight velocity and temperature as functions of position and time thus identifying transverse magnetohydrodynamic waves pervading the superpenumbral fibrils. These waves are characterized by the periods of 2.5 to 4.5 minutes, and the propagation direction parallel to the fibrils, the supersonic propagation speeds of 45 to 145 km s<sup>-1</sup>, and the close association with umbral oscillations and running penumbral waves in sunspots.

Chai et al. (2022) studied sunspot oscillations and wave propagation in NOAA AR 12470 using ALMA, GST, SDO, and IRIS data. The 2 s cadence ALMA images allowed them to resolve 3 minute oscillations in the sunspot chromosphere. Fourier analysis, applied to ALMA Band 3 (100 GHz, 3 mm) and GST H $\alpha$  data, revealed that ALMA temperature fluctuations are consistent with those expected for a propagating acoustic wave, with a slight asymmetry indicating nonlinear steepening.

## 6. EVOLUTION OF ACTIVE REGIONS

Zheng et al. (2020) studied the formation of the tiny flux rope in the center of an active region (AR) that was closely associated with continuous magnetic flux emergence, convergence, and cancellation in the photosphere.

## 7. FILAMENTS AND PROMINENCES

Using FISS data Park et al. (2013) determined the temperature and non-thermal velocities of plasma in solar prominences to be within 4-20 kK and 4-11 km s<sup>-1</sup> ranges. We also found strong temperature variations from one location to another within a prominence.

Zou et al. (2016) observed cool H $\alpha$  material being injected into an AR filament at a speed of 5-10 km s<sup>-1</sup>. The source of the injection was associated with a brightenings and magnetic cancellation implying the importance of magnetic reconnection in replenishing the filament with plasmas from the lower atmosphere. Counterstreaming plasma were detected near one endpoint of the filament, with the plane-of-the-sky speed being 7-9 km s<sup>-1</sup> as measured using H $\alpha$  red-wing filtergrams and 9-25 km s<sup>-1</sup> in the blue-wing filtergrams. The observa-

Figure 1. from Spectroscopic Detection of Alfvénic Waves in the Chromosphere of Sunspot Regions  
 null 2021 APJL 914 L16 doi:10.3847/2041-8213/ac052b  
 http://dx.doi.org/10.3847/2041-8213/ac052b

© 2021. The American Astronomical Society. All rights reserved.

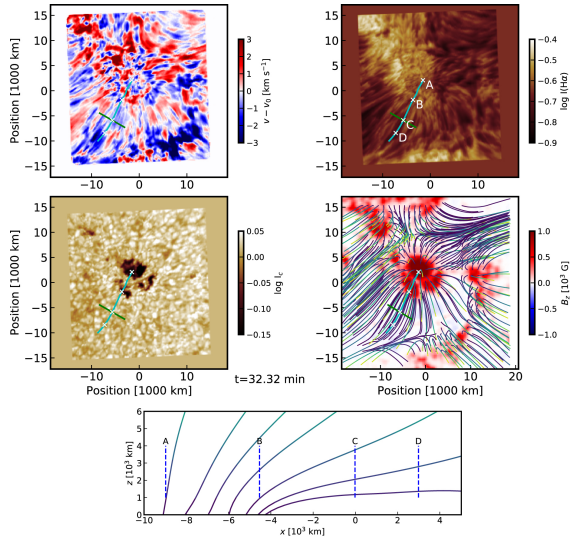


**Figure 19.** Maps of line-of-sight velocity (upper left), H $\alpha$ line center intensity (upper right), continuum intensity (middle left) constructed from a single raster scan observation of the FISS, and the line-of-sight magnetogram (middle right) with the lines of extrapolated linear-force-free magnetic fields projected on the observing plane. The lower-lying parts of the field lines are marked in darker colors, and the upper-lying parts in brighter colors. Note that the velocity data presented in the map have been high-pass filtered for oscillations of period  $<16$  minutes. The cyan curve in each map represents the original cut used for the construction of the spacetime plots, and the green line in each map does another cut perpendicular to the original slit. The point of intersection is used to define the origin of the localized Cartesian coordinates for the measurement. The x coordinate increases to the lower left along the cyan curve, and the y coordinate, to the lower right along the green curve. The four locations of interest are marked by the symbols. Bottom: the side view of the extrapolated magnetic field lines. Each vertical dashed line indicates the x value and the supposed z range (1000 to 4000 km) in each location. An animation of the top four panels is available. The animation runs from  $t = 0$  to 44.43 minutes. The realtime duration of the animation is 75 s. Adopted from [Chae et al. \(2021\)](#).

tions are indicative that this active region filament was supported by a sheared arcade without magnetic dips, and the counter-streaming were due to unidirectional flows with alternative directions, rather than due to the longitudinal oscillations of filament threads as in many other filaments.

[Joshi et al. \(2016\)](#) observed oscillations in several thin and long features connecting the filament spine to the chromosphere below. Small-scale magnetic flux cancellation accompanied by a brightening was observed at the footpoint of the features shortly before their appearance. A slow rise of the filament was detected in addition to the oscillations, indicating a gradual loss of equilibrium. Their analysis indicates that a change in magnetic field connectivity between two neighbouring active regions and the quiescent filament resulted in a weakening of the overlying arcade of the filament, leading to its eruption. It is also suggested that the oscillating features are filament barbs, and the oscillations are a manifestation during the pre-eruption phase of the filaments.

[Li et al. \(2017\)](#) presented detailed observations of a pre-eruption evolution of a filament with persistent downflows along the H $\alpha$ multi-threaded component of the filament toward one of the endpoints. Authors attributed the observed downflows to the plasma draining effect causing the filament rising prior to its eruption. During the slow-rise phase, the downflows drained away  $\sim 10^{15}$  g of mass over a few hours, which is believed to be essential for the instability, and could be an important precursor of eruptive events.

[Wang et al. \(2018a\)](#) observed counter-streaming motions in an circular AR filament rooted in an LB. The apparent speed of the flow was about  $10\text{-}60$  km  $\text{s}^{-1}$ . The most intriguing findings were the associated magnetic structures and counter-streaming motions in the LB. Similar to those of the filament, the magnetic field showed a dominant transverse component in the LB. However, the filament was located between opposite magnetic polarities, while the LB was located between strong fields of the same polarity. Authors analyzed the power of oscillations and found that the counter-streaming within the filament was due to physical mass motion along fibrils, while that of the LB was due to oscillations along the line-of-sight. The oscillation power peaked at about 4 min. However, a section of the LB also includes an extension of the filament indicating that some strands of the filament are extended to and rooted in that part of the light bridge.

[Wang et al. \(2018d\)](#) argued that cool material in the low atmosphere can be directly injected into the upper atmosphere and jets may be triggered due to magnetic reconnection between pre-existing and emerging magnetic fields. Authors further conclude that jets may not only supply material for the filament, but they also may inject helicity into the filament. The estimated mass loading by jets is sufficient to account for the mass of the filament.

[Zou et al. \(2019\)](#) discussed the possibility of filament material replenishment in a weak magnetic field. It was argued that the local plasma can be heated to up to about 1.3 times of the original temperature, which results in an acceleration of about  $-0.017$  km  $\text{s}^{-2}$ . It can lift dense plasma up to at least 10 Mm along field lines

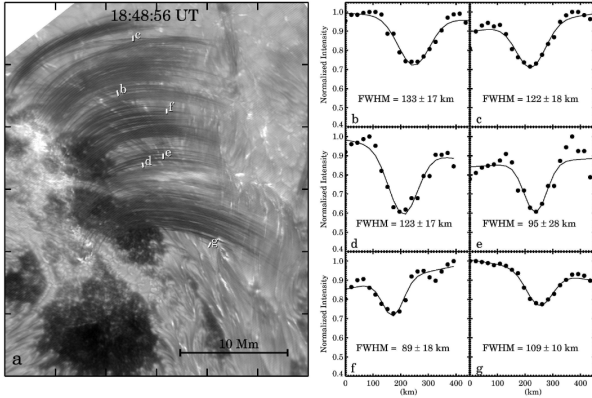


**Figure 20.** Panel a: a snapshot of  $H\alpha+0.1$  nm image taken in the decay phase of the flare. Six short slits mark where the cross-section of six loops were measured. Panels b-g: the normalized  $H\alpha+0.1$  nm intensity profiles (black dots) along the slits and the Gaussian fits (black curves). The six slits in panel a are distinguished by labelling with panel letters “b” through “g”. The Gaussian FWHM and its  $\pm 3\sigma$  are provided in each panel. Adopted from [Jing et al. \(2016\)](#).

with an inclination angle smaller than  $50^\circ$ , which is the typical height of AR filaments. At the same time, the model showed that this mechanism can not inject plasma higher than 25 Mm in case of quiescent filaments, where the magnetic field is more vertical.

## 8. SOLAR FLARES

[Sharykin and Kosovichev \(2014\)](#) reported previously unresolved sub-arcsecond structure of flare ribbons in regions of strong magnetic field consisting of numerous small-scale bright knots. They observed a red-blue asymmetry of in the  $H\alpha$  flare ribbons with a width of about 100 km and argued that Joule heating can be responsible for the enhanced  $H\alpha$  knots in the ribbons.

[Zeng et al. \(2014\)](#) reported that the triplet states of the 1083 nm multiplet are populated via photoionization of chromospheric plasma followed by radiative recombination. Surprisingly, the He II 30.4 nm line is reasonably well matched by the standard emission measure calculations, along with the C IV emission which dominates the AIA 160 nm channel during flares.

[Kumar et al. \(2015\)](#) reported direct evidence of chromospheric reconnection at the polarity inversion line between two small opposite polarity sunspots that resulted in a slow rise of untwisting jets and a two-ribbon flare. The reconnection also formed a chromospheric flux rope during the first M1.0 flare and its subsequent eruption/disruption during the second C8.5 flare.

[Yurchyshyn et al. \(2015b\)](#) presented evidence of the flare and eruption being directly triggered by flux emergence that occurred inside a  $\delta$ -sunspot at a LB separating two opposite polarity umbral cores.

[Lim et al. \(2016\)](#) studied a sequence of flares driven by continuous emergence of a magnetic bubble and he-

licity injection. Each flare developed a jet structure that evolved in a manner similar to evolution of the blowout jet and after that more jets appeared to form a curtain-like structure that consisted of many fine threads accompanied by subsequent brightenings near the footpoints of the fine threads.

[Xu et al. \(2016\)](#) detected in He I 1083 nm data a striking “negative” flare with a narrow ( $\sim 340$  km) but unambiguous “dark” moving front. Such negative contrast can be produced in He I 1083 nm under special circumstances by non-thermal electron collisions or photoionization followed by recombination.

[Hong et al. \(2016\)](#) analysed both spectroscopic and imaging observations of magnetic reconnection in the chromosphere leading to a micro-flare. Three-dimensional nonlinear force-free field modeling revealed twisted field lines (a flux rope) at a low altitude, co-spatial with the dark threads seen in He I 1083 nm images. The instability of the flux rope may have initiated flare-related reconnection. These observations provide clear evidence of magnetic reconnection in the chromosphere and show the similar mechanisms of a microflare to those of major flares.

[Jing et al. \(2016\)](#) measured the cross-sectional widths of flare ribbons, post-flare loops and footpoint brightenings, which generally lie in the range of 80-200 km, well below the resolution of most current instruments (Figure 20). Confining the scale of such fine structure provides an essential piece of information in modeling the energy transport mechanism of flares, which is an important issue in solar and plasma physics.

[Cho et al. \(2016\)](#) reported a significant and rapid pre-flare  $H\alpha$  line broadening extending toward both line wings up to  $-0.45$  nm and  $0.2$  nm, which implies a mixture of velocities in the range of  $-130$  km  $s^{-1}$  to  $38$  km  $s^{-1}$  derived by applying the cloud model. The blueshifted broadening lasted for about six minutes and was temporally and spatially correlated with the onset of a rising filament.

[Wang et al. \(2016\)](#) for the first time analysed sunspot dynamics during flaring using He I 10830 Å narrow-band imaging. The most prominent feature is the sudden appearance of an oscillating absorption strip inside a flare ribbon when it sweeps across the sunspot’s penumbra and umbral. Authors suggest that this is the result of a sudden increase in the density of ortho-helium atoms in the area of the sunspot being excited by the flare’s extreme ultraviolet illumination. This explanation is based on the observation that 10830 Å absorption around the sunspot area gets enhanced during the flare.

[Yurchyshyn et al. \(2017\)](#) studied fine spatial and temporal details of an M1.3 white-light (WL) flare observed in close proximity to the west solar limb. The TiO WL flare consisted of compact and intense cores surrounded by less intense spatial halos. The strong and compact WL cores were measured to be  $\approx 0''.2$  across, with an area of about  $10^{14}$  cm $^2$ . Several TiO features

were not cospatial with  $H\alpha$  flare ribbons and were displaced toward the disk center by about 500 km, which suggests that the TiO and  $H\alpha$  radiation probably did not originate in the same chromospheric volume. The observed TiO intensity enhancements are not normally distributed and are structured by the magnetic field of the penumbra.

Wang et al. (2017) studied flare precursors that were initiated at a small-scale magnetic channel with multiple polarity inversions and enhanced magnetic fluxes and currents, lying near the footpoints of sheared magnetic loops. Microwave spectra corroborated that these precursor emissions originate in the atmosphere. These results provide evidence of low-atmospheric small-scale energy release, possibly linked to the onset of the main flare.

Sharykin et al. (2017) studied interaction of two magnetic flux ropes with oppositely directed magnetic fields at the polarity inversion line (PIL). These flux ropes are observed as a compact sheared arcade along the PIL. GST  $H\alpha$  data revealed the formation of a thin three-ribbon structure corresponding to a small-scale photospheric magnetic arcade. The observational results are evidence in favor of the primary energy release site located in the chromospheric plasma with strong electric currents concentrated near the PIL. In this case, magnetic reconnection is triggered by the interacting magnetic flux ropes forming a current sheet elongated along the PIL.

Kumar et al. (2017) reported direct evidence of merging and reconnection of cool  $H\alpha$  loops in the chromosphere during two homologous flares caused by a shear motion at the footpoints of two loops. The reconnection formed an unstable flux rope with counterclockwise rotation. The flux rope could not reach the height of torus instability and failed to form a coronal mass ejection. The HMI magnetograms revealed rotation of the negative and positive polarity sunspots in the opposite directions, while rapid photospheric flux cancellation (duration 20-30 min, rate  $\approx 3.44 \times 10^{20}$  Mx/h) was observed during the event and X-ray RHESSI sources were located at the site of the loop coalescence.

Yan et al. (2017) observed emergence of a small-scale flux rope near a large sunspot that triggered an M-class flare and a coronal mass ejection. During the emergence rotation of satellite sunspots was observed at the footpoints of the flux rope. The free energy that the flux rope injected into the system was sufficient to power the M-class flare.

Su et al. (2018) studied magnetic configuration and evolution of an active region by constructing coronal magnetic field models based on SDO/HMI magnetograms using two independent methods, i.e., the nonlinear force-free field (NLFFF) extrapolation and the flux rope insertion method. The models consist of multiple flux ropes with mixed signs of helicity, which is consistent with the GST observations of multiple fila-

ment bundles. The footprints of quasi-separatrix layers (QSLs) derived from the extrapolated NLFFF compare favorably with the observed flare ribbons. Based on the model data authors concluded that these circular shaped flares are caused by 3D magnetic reconnection at the QSLs associated with the AFS possessing mixed signs of helicity.

Yang et al. (2018) developed an automated solar flare detection method using an adaptive gray threshold and an area threshold. Extensive testing verified that the proposed method can obtain more stable and accurate segmentation results on full disk  $H\alpha$  images and satisfying segmentation results on high-resolution GST  $H\alpha$  images.

Wang et al. (2018e) used 1083 nm images to detect below the horizontal fibrils of the filament spine a sheared arch filament system (AFS) lying across the penumbra and surrounding satellite sunspots. Three microflares occurred before the eruption and were followed by the appearance of three EUV hot channels. The 1083 nm imaging enabled authors to trace the first two hot channels to their very early stage, which is signified by the rising of the AFS after the first two precursors. Continuous flux emergence and localized flare-associated cancellation were observed under the AFS. These observations support the fact that the hot channels are the result of magnetic reconnections during precursors.

Liu et al. (2018) found that changes of photospheric fields occur at the arrival of the flare ribbon front, thus propagating analogously to flare ribbons (Figure 21). In general, the horizontal field increases and the field lines become more inclined to the surface. When ribbons sweep through regions that undergo a rotational motion, the fields transiently become more vertical with decreased horizontal field and inclination angle, and then restore and/or become more horizontal than before the ribbon arrival. Authors conclude that photospheric fields respond nearly instantaneously to magnetic reconnection in the corona.

Wang and Liu (2019) reviewed high resolution observations and properties of magnetic flux ropes (MFR), which are consistent with those inferred from nonlinear force-free field extrapolations. Authors also discuss evidence that MFRs may exist in the photosphere. The magnetic channel structure with multiple polarity inversions and only discernible in high-resolution magnetograph data, may be a signature of these photospheric MFRs. They are likely to form below the surface and appear in the photosphere through flux emergence. Triggering of some solar eruptions may thus be associated with an enhanced twist in the low-atmospheric MFRs (see also Toriumi and Wang 2019, for review of flare productive ARs).

Huang et al. (2019) found that Mg II lines measured at the leading edge of propagating flare ribbons are characterized by blue-wing enhancement and strong broadening. On the other hand, redshifts in Mg II and  $H\alpha$

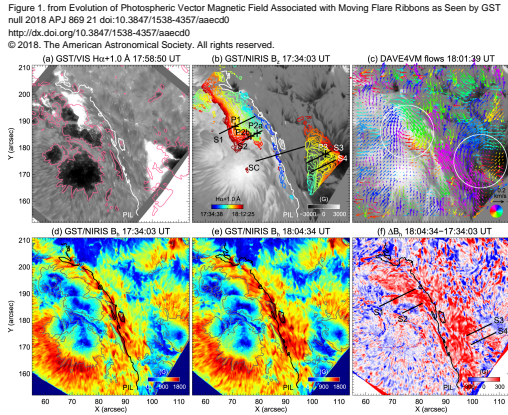


**Figure 21.** Evolution of flare ribbons and magnetic fields. (a)  $H\alpha+0.1$  nm image near the flare peak showing the two major flare ribbons. The magenta lines contour Bz map (smoothed by a window of  $0''.7\times 0''.7$ ) at  $\pm 1600$  G. (b) Bz image superimposed with curves (color-coded by time) that depict the progression of flare ribbon fronts. Note that the western ribbon and its evolution are not entirely captured due to the limited FOV of GST. The overplotted lines S1-S4 and SC indicate the slit positions of the time slices and vertical cross sections shown in Figures 2 and 5, respectively. The magnetic field evolution in several sample positions (P1, P2a, P2b, and P3) is plotted in Figure 3. (c) Bz image superimposed with arrows (color-coded by direction; see the color wheel) that illustrate DAVE4VM flows averaged between 17:52:56 and 18:13:17 UT subtracted by the flow field averaged between 17:32:35 and 17:51:29 UT. The two white circles mark the regions of rotational motion. A window size of 23 pixels was set for DAVE4VM tracking. (d)-(f) Maps of Bh in the pre- and post-flare states and their difference. The PIL is overplotted in (a)-(b) and (d)-(f). All the images in this paper are aligned with respect to 17:34:03 UT. Adopted from Liu et al. (2018).

are found in the trailing areas of flare ribbons. Numerical modeling results, produced by combining RADYN and RH models, suggest that the Mg II line broadening is possibly caused by unresolved turbulence with velocities about 10 to 30  $\text{km s}^{-1}$ . The enhanced blue wing is likely due to a decrease of temperature and an increase of electron density, as consequences of electron precipitation.

Zuo et al. (2019) observed a solar jet originating from a satellite sunspot, which has gradually decayed during the jet event. Its area was reduced by about 80% by the end of the jet activity. Multi-wavelength observations of the photosphere, the chromosphere, and the corona suggest that magnetic cancellations in the middle or lower chromosphere may be the trigger of the solar jet event.

Liu et al. (2016) observed the sudden flare-induced rotation of a sunspot. The rotation was non-uniform

over the sunspot: as the flare ribbon swept across, different parts of the sunspot accelerate (up to  $\sim 50^\circ/\text{h}$ ) at times corresponding to peaks of flare hard X-ray emission. The rotation may be driven by the surface Lorentz-force change due to the back reaction of coronal magnetic restructuring and is accompanied by a downward Poynting flux. Rapid and irreversible changes of the sunspot penumbra and umbra associated with an eruptive flare were also observed in (Yurchyshyn et al. 2015b, Fig. 3).

Xu et al. (2018) detected a sudden rotation of vector magnetic fields, about  $12\text{-}20^\circ$  counterclockwise, associated with a flare. Unlike the permanent changes reported previously, the azimuth-angle change is transient and cospatial/temporal with  $H\alpha$  emission. The resulting azimuth angle becomes closer to that in potential fields suggesting untwist of flare loops. The magnetograms were obtained in the near infrared at  $1.56 \mu\text{m}$ , which is minimally affected by flare emission and no intensity profile change was detected. We believe that these transient changes are real and discuss the possible explanations in which the high-energy electron beams or Alfvén waves play a crucial role.

Huang et al. (2020) studied the evolution of the He I 10830Å emission obtained from RADYN model and compared it with observations. Models had the injected electron spectra parameters close to observational estimates. The modeling results agree well with observations, in the sense of both the maximum intensity decrease ( $-17.1\%$ , compared with the observed value of  $-13.7\%$ ) and the trend of temporal variation (initial absorption phase followed by the emission).

Wang et al. (2020b) reported a heating event of a flare arcade that was closely associated with two rapid contractions of the overlying filament threads during the partial eruption of the filament. The contractions were discernible in He I 10830 Å images and have signatures in AIA EUV data. The two rapid contractions resulted from a sudden drop in magnetic pressure after the eruption of two hot channels. Clear evidence suggests that magnetic reconnection may occur between the contracting filament threads and the low-lying magnetic field.

Wei et al. (2021) report microwave imaging spectroscopy observations of an M1.4-class solar flare associated with a partial eruption of a twisted filament. The extreme ultraviolet (EUV) and X-ray signatures of the event are generally consistent with the standard scenario of eruptive flares, with the presence of double flare ribbons connected by a bright flare arcade. Intriguingly, this partial eruption event features a microwave counterpart, whose spatial and temporal evolution closely follow the filament seen in  $H\alpha$  and EUV. The spectral properties of the microwave source are consistent with nonthermal gyrosynchrotron radiation. Authors derived the magnetic field strength along the filament spine, which ranges from 600 to 1400 Gauss from its apex to the legs. The results agree well with the nonlinear

Figure 9. from Coronal Magnetic Field Measurements along a Partially Erupting Filament in a Solar Flare  
 null 2021 APJ 923 213 doi:10.3847/1538-4357/ac2999  
 http://dx.doi.org/10.3847/1538-4357/ac2999  
 © 2021. The Author(s). Published by the American Astronomical Society.

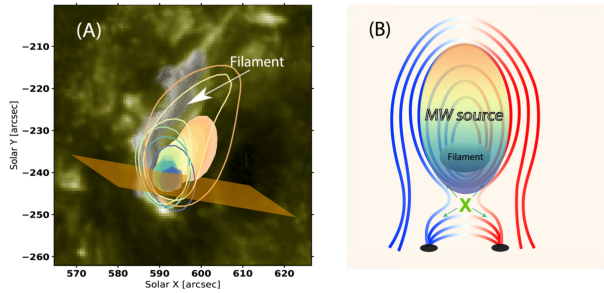


**Figure 22.** Schematic cartoon that shows the relationship between the filament and the microwave source. (A) Multifrequency EOVS A microwave images (preflare background subtracted) at 19:24:00 UT. Open and filled contours are 50% and 90% of the maximum, respectively. Background is the SDO/AIA 1600Å image at the moment and the filament shown is extracted from the BBSO/GST Hα image. (B) Schematic cartoon of the cross-section of the flux rope, at a location indicated by the orange surface in (A). Adopted from Wei et al. (2021).

force-free magnetic model extrapolated from the preflare photospheric magnetogram. We conclude that the microwave counterpart of the erupting filament is likely due to flare-accelerated electrons injected into the filament-hosting magnetic flux rope cavity following the newly reconnected magnetic field lines.

Xu et al. (2022) observed enhanced absorption the flare ribbon’s leading edge in the center of the He I 10830 Å line, while the rest of the ribbon was observed to be in emission. Two types of spectra, a “convex” shaped with higher intensity at line core and a “concave” shaped with higher emission in the line wings, were found at the trailing and peak flaring areas, respectively. These observations strongly suggests that the negative flares observed in He I 10830 Å with mono-filtergram previously were not caused by pure Doppler shifts of this spectral line. Instead, the enhanced absorption appears to be a consequence of flare-energy injection, namely non-thermal collisional ionization of helium caused by the precipitation of high-energy electrons, as found in our recent numerical modeling results.

Shen et al. (2022) observed that during the precursor phase of the X1.6 class flare on 2014 September 10, magnetic reconnection first occurred between one of the two J-shaped magnetic flux ropes, which were parts of a sigmoid. At the same time, photospheric vertical electric currents (VEC) in that area began to increase. GST He I 10830 Å data revealed a narrow absorption (dark) front that ran along the erupting magnetic structure (or

the erupting hot channel) and moved in the direction of the eruption during the precursor phase. Assuming the excitation mechanism of Helium atoms along the absorption front by non-thermal electrons, the phenomenon shows that the interaction between the erupted hot channel and the overlying (or surrounding) magnetic field has yielded electron acceleration.

## 9. INSTRUMENTATION, DATA PROCESSING, NUMERICAL TOOLS, AND MACHINE LEARNING

Yang et al. (2020) described the CrYogenic solar spectrograph (CYRA), which is a GST facility instrument. CYRA focuses on the study of the near-infrared solar spectrum between 1 and 5 microns, an under-explored region which is not only fertile ground for photospheric magnetic diagnostics but also allows a unique window into the chromosphere lying atop the photosphere. CYRA is the first-ever fully cryogenic spectrograph in any solar observatory with its two predecessors, on the McMath-Pierce and Mees Telescopes, being based on warm optics except for the detectors and order sorting filters. CYRA is used to probe magnetic fields in various solar features and the quiet photosphere. CYRA measurements will allow new and better 3D extrapolations of the solar magnetic field and will provide more accurate boundary conditions for solar activity models. The superior spectral resolution of 150,000 and better allows enhanced observations of the chromosphere in the carbon monoxide (CO) spectral bands and will yield a better understanding of energy transport in the solar atmosphere. CYRA is divided into two optical sub-systems: The Fore-Optics Module and the Spectrograph. The Spectrograph is the heart of the instrument and contains the IR detector, grating, slits, filters, and imaging optics all in a cryogenically cooled Dewar (cryostat). The sensor is a 2048 by 2048 pixel HAWAII 2 array produced by Teledyne Scientific and Imaging, LLC. The cryostat interior and the readout electronics are maintained at 90 Kelvin by helium refrigerant-based cryo-coolers, while the IR array is cooled to 30 Kelvin. The Fore-Optics Module de-rotates and stabilizes the solar image, provides scanning capabilities and transfers the GST image to the Spectrograph. CYRA has been installed and is undergoing its commissioning phase. This paper reports on the design, implementation, and operation of CYRA in detail. The preliminary scientific results have been highlighted as well.

Schmidt et al. (2020) performed an on-sky MCAO experiment using 4 deformable mirrors (DMs) to analyze the relevance of their sequence to the residual wavefront error. Two DMs were conjugate to 4 and 8 km. The other two DMs were placed in pupil images upstream and downstream of the 4-km and 8-km mirrors. At any time, both high altitude DMs were active but only one pupil DM was active while the other one stayed flat. Firstly, we found that the MCAO control loops using ei-

ther pupil DM were stable and robust. Dynamic misregistration, which was present for the first pupil DM, was not an immediate problem for the controller. We did not notice an apparent difference when repeatedly switching between the pupil DMs during the operation. A closer analysis of the contrast in the corrected images and AO telemetry indicates an advantage when the pupil correction was applied with the DM that was downstream of the high-altitude DMs. This finding is consistent in several data recorded at different days. The difference, however, is small. A more detailed analysis is probably needed to rule out error sources potentially not considered herein to draw a final conclusion on the optimal sequence of DMs in MCAO and its practical relevance.

Chae et al. (2020) developed a multilayer spectral inversion technique based on an assumption that the atmosphere consists of a finite number of layers. In each layer the absorption profile is constant and the source function varies with optical depth with a constant gradient. Authors considered a three-layer model of radiative transfer where the lowest layer is identified with the photosphere and the two upper layers are identified with the chromosphere. This three-layer model is fully specified by 13 parameters. Authors report that the model successfully fits most of the observed profiles and produces regular maps of the model parameters. The combination of the inferred Doppler widths of the two lines yields reasonable estimates of temperature and nonthermal speed in the chromosphere.

Liu et al. (2020) proposed a new machine-learning approach to Stokes inversion based on a convolutional neural network (CNN) and the Milne-Eddington (ME) method. By learning the latent patterns in the training data prepared by the physics-based ME tool, the proposed CNN method is able to infer vector magnetic fields from the Stokes profiles. The CNN method produces smoother and cleaner magnetic maps than the widely used ME method. Furthermore, the CNN method is four to six times faster than the ME method and able to produce vector magnetic fields in nearly real time, which is essential to space weather forecasting.

Xu et al. (2021) studied characteristics of isolated multiwavelength BPs using the cotemporal and cospatial TiO band and H $\alpha$  line wings. A deep-learning (DL) method, based on Track Region-based Convolutional Neural Networks, was proposed to detect, segment, and match the BPs across multiple wavelength observations.

Bai et al. (2021) proposed a new method to quickly estimate the unsigned radial component of the magnetic field,  $|Br|$ , and the transverse field,  $B_t$ , from photospheric continuum images (I) using CNN methods. The CNN models can successfully estimate  $|Br|$  as well as  $B_t$  maps in sunspot umbra, penumbra, pore, and strong network regions based on the evaluation of four active regions (test datasets). The method can be applied to the reconstruction of the historical magnetic fields and

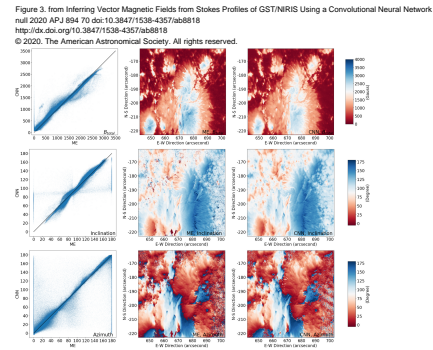


**Figure 23.** Comparison between the ME and CNN methods for deriving  $B_{total}$ ,  $\phi$  (inclination angle), and  $\theta$  (azimuth angle) based on the test image from AR 12371 collected on 2015 June 25 20:00:00 UT, where training data were taken from AR 12371 on 2015 June 22. Displayed from top to bottom are the results for  $B_{total}$ ,  $\phi$  (inclination angle), and  $\theta$  (azimuth angle). The first column shows scatter plots where the X-axis and Y-axis represent the values obtained by the ME and CNN methods, respectively. The black diagonal line in each scatter plot corresponds to pixels whose ME-calculated values are identical to CNN-inferred values. The second column shows magnetic maps derived by the ME method. The third column shows magnetic maps inferred by our CNN method. Adopted from Liu et al. (2020).

to future observations for providing the quick look data of the magnetic fields.

Jiang et al. (2021) presented a new DL method, FibrilNet, for tracing chromospheric fibrils in chromospheric H $\alpha$  images. The approach consists of i) a data pre-processing component that prepares a training data set, ii) a DL model implemented as a Bayesian convolutional neural network for probabilistic image segmentation, and iii) a post-processing component containing a fibril-fitting algorithm to determine fibril orientations.

Abduallah et al. (2021) presented a machine-learning-as-a-service (MLaaS) framework, called DeepSun, for predicting solar flares based on HMI data products. A training data set was constructed by utilizing physical parameters provided by HMI-SHARP data. The DeepSun system employs several ML algorithms and provides an application programming interface (API) for remote programming users. To our knowledge, DeepSun is the first web-based MLaaS tool capable of predicting solar flares.

Deng et al. (2021) used the Generative Adversarial Network (GAN) and HMI and GST data to construct a precisely aligned data set based on the scale-invariant feature transform algorithm and to reconstruct the HMI continuum images with four times better resolution. Neural networks based on the conditional GAN and self-attention mechanism were trained to restore the details of solar active regions and to predict the reconstruction

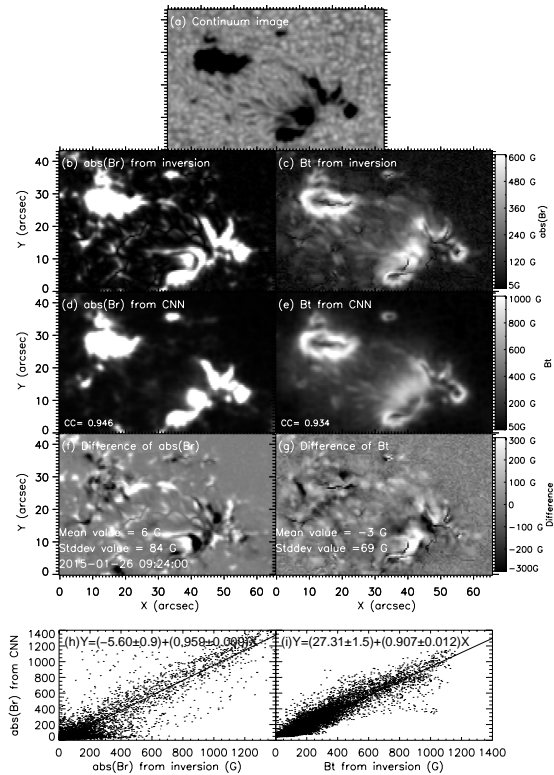


**Figure 24.** Result from SHARP No. 5118. Panels a–c: image of continuum,  $|Br|$ , and Bt from Stokes inversion, respectively. The unsigned Br and Bt estimated from panel a with our CNN model are shown in panels d and e. Panel f is the difference map of  $|Br|$  between Stokes inversion and CNN model, while panel g is that of Bt. Panels h and j: scatter plots of  $|Br|$  and Bt between the two methods. Adopted from Bai et al. (2021).

error. The experimental results show that the reconstructed images are in good agreement with GST images, demonstrating the success of resolution improvement using ML.

Yang et al. (2022a) designed an automated method to detect post flare loops (PFLs, or post eruption arcade). First, straight lines are detected using an edge-detection tool, and then a curve-growing technique is utilized. The grown curves were screened to eliminate isolated and intersected curves. Method validation, using GST red wing H $\alpha$  images, showed that it can effectively detect PFLs at all stages of their evolution. Based on the recognition results, authors report that the auto-

matically computed loop width of  $118 \pm 35$  km is consistent with previously reported width of  $124 \pm 19$  km.

Liang et al. (2022) proposed a novel coarse-to-fine solar image registration method to register the multichannel solar images. In the coarse registration step, authors used the regular step gradient descent algorithm as an optimizer to maximize the normalized cross correlation metric. The fine registration step uses the Powell-Brent algorithms as an optimizer and brings the Mattes mutual information similarity metric to the minimum. Five pairs of images with different resolutions, rotation angles, and shifts were selected to compare and evaluate the method. The image pair included GST and HMI data. The test proved that the proposed method not only reaches better registration precision but also has better robustness.

Yang et al. (2022b) developed a Python language package for registration of ground-based high-resolution imaging data acquired by GST to space-based full-disk continuum intensity data provided by SDO with the scale-invariant feature transform method. The package also includes tools to align data sets obtained in different wavelengths and at different times utilizing the optical flow method. We present the image registration and coalignment workflow. The alignment accuracy of each alignment method is tested with the aid of radiative magnetohydrodynamics simulation data. We update the pointing information in GST data fits headers and generate GST and SDO imaging data products as science-ready four-dimensional data cubes.

Jiang et al. (2022) presented a new deep learning method, named Stacked Deep Neural Networks (SDNN), for inferring line-of-sight (LOS) velocities and Doppler widths from Stokes profiles collected by NIRIS. The training data for SDNN are prepared by a Milne-Eddington (ME) inversion code used by BBSO. The SDNN-inferred LOS velocities are highly correlated with the ME-calculated ones with the Pearson product-moment correlation coefficient being close to 0.9 on average. Second, SDNN is faster, while producing smoother and cleaner LOS velocity and Doppler width maps, than the ME inversion code. Third, the maps produced by SDNN are closer to ME's maps than those from the related ML algorithms, demonstrating that the learning capability of SDNN is better than those of the ML algorithms.

*Facility:* GST

## REFERENCES

- V. Abbasvand, M. Sobotka, M. Švanda, P. Heinzel, M. García-Rivas, C. Denker, H. Balthasar, M. Verma, I. Kontogiannis, J. Koza, D. Korda, and C. Kuckein. Observational study of chromospheric heating by acoustic waves. *A&A*, 642:A52, Oct. 2020. <https://doi.org/10.1051/0004-6361/202038559>.
- Y. Abdullah, J. T. L. Wang, Y. Nie, C. Liu, and H. Wang. DeepSun: machine-learning-as-a-service for solar flare prediction. *Research in Astronomy and Astrophysics*, 21(7):160, Aug. 2021. <https://doi.org/10.1088/1674-4527/21/7/160>.

- V. Abramenko, V. Yurchyshyn, P. Goode, and A. Kilcik. Statistical Distribution of Size and Lifetime of Bright Points Observed with the New Solar Telescope. *ApJL*, 725(1):L101–L105, Dec. 2010. <https://doi.org/10.1088/2041-8205/725/1/L101>.
- V. I. Abramenko. Diagnostics of turbulent and fractal properties of photospheric plasma outside active regions of the Sun. *Geomagnetism and Aeronomy*, 56(7): 842–847, Dec. 2016. <https://doi.org/10.1134/S0016793216070021>.
- V. I. Abramenko and V. B. Yurchyshyn. Analysis of quiet-sun turbulence on the basis of SDO/HMI and goode solar telescope data. *MNRAS*, 497(4):5405–5412, Oct. 2020. <https://doi.org/10.1093/mnras/staa2427>.
- V. I. Abramenko, V. Carbone, V. Yurchyshyn, P. R. Goode, R. F. Stein, F. Lepreti, V. Capparelli, and A. Vecchio. Turbulent Diffusion in the Photosphere as Derived from Photospheric Bright Point Motion. *ApJ*, 743(2):133, Dec. 2011. <https://doi.org/10.1088/0004-637X/743/2/133>.
- V. I. Abramenko, V. B. Yurchyshyn, P. R. Goode, I. N. Kitiashvili, and A. G. Kosovichev. Detection of Small-scale Granular Structures in the Quiet Sun with the New Solar Telescope. *ApJL*, 756(2):L27, Sept. 2012. <https://doi.org/10.1088/2041-8205/756/2/L27>.
- V. I. Abramenko, G. P. Zank, A. Dosch, V. B. Yurchyshyn, P. R. Goode, K. Ahn, and W. Cao. Characteristic Length of Energy-containing Structures at the Base of a Coronal Hole. *ApJ*, 773(2):167, Aug. 2013. <https://doi.org/10.1088/0004-637X/773/2/167>.
- K. Ahn, J. Chae, K.-S. Cho, D. Song, H. Yang, P. R. Goode, W. Cao, H. Park, J. Nah, B.-H. Jang, and Y.-D. Park. Active Region Coronal Rain Event Observed by the Fast Imaging Solar Spectrograph on the NST. *SoPh*, 289(11):4117–4136, Nov. 2014. <https://doi.org/10.1007/s11207-014-0559-x>.
- A. Andić, P. R. Goode, J. Chae, W. Cao, K. Ahn, V. Yurchyshyn, and V. Abramenko. Oscillatory Behavior in the Quiet Sun Observed with the New Solar Telescope. *ApJL*, 717(2):L79–L82, July 2010. <https://doi.org/10.1088/2041-8205/717/2/L79>.
- A. Andić, J. Chae, P. R. Goode, W. Cao, K. Ahn, V. Yurchyshyn, and V. Abramenko. Response of Granulation to Small-scale Bright Features in the Quiet Sun. *ApJ*, 731(1):29, Apr. 2011. <https://doi.org/10.1088/0004-637X/731/1/29>.
- A. Andić, J. Chae, H. Park, H. Yang, K. Ahn, W. Cao, and Y. D. Park. Connection Between Chromospheric Events and Photospheric Dynamics. *SoPh*, 288(1):55–71, Nov. 2013. <https://doi.org/10.1007/s11207-012-0113-7>.
- X. Bai, H. Socas-Navarro, D. Nóbrega-Siverio, J. Su, Y. Deng, D. Li, W. Cao, and K. Ji. Signatures of Magnetic Reconnection at the Footpoints of Fan-shaped Jets on a Light Bridge Driven by Photospheric Convective Motions. *ApJ*, 870(2):90, Jan. 2019. <https://doi.org/10.3847/1538-4357/aaf1d1>.
- X. Bai, H. Liu, Y. Deng, J. Jiang, J. Guo, Y. Bi, T. Feng, Z. Jin, W. Cao, J. Su, and K. Ji. A deep learning method to estimate magnetic fields in solar active regions from photospheric continuum images. *A&A*, 652:A143, Aug. 2021. <https://doi.org/10.1051/0004-6361/202140374>.
- X. Y. Bai, J. T. Su, W. D. Cao, S. Q. Liu, Y. Y. Deng, and T. G. Priya. Multi-wavelength Observations of a Subarcsecond Penumbral Transient Brightening Event. *ApJ*, 823(1):60, May 2016. <https://doi.org/10.3847/0004-637X/823/1/60>.
- W. Cao, Z. Ning, P. R. Goode, V. Yurchyshyn, and H. Ji. Evidence of Filament Upflows Originating from Intensity Oscillations on the Solar Surface. *ApJL*, 719(1):L95–L98, Aug. 2010. <https://doi.org/10.1088/2041-8205/719/1/L95>.
- J. Chae and Y. E. Litvinenko. Nonlinear Effects in Three-minute Oscillations of the Solar Chromosphere. I. An Analytical Nonlinear Solution and Detection of the Second Harmonic. *ApJ*, 844(2):129, Aug. 2017. <https://doi.org/10.3847/1538-4357/aa7be9>.
- J. Chae, P. R. Goode, K. Ahn, V. Yurchyshyn, V. Abramenko, A. Andić, W. Cao, and Y. D. Park. New Solar Telescope Observations of Magnetic Reconnection Occurring in the Chromosphere of the Quiet Sun. *ApJL*, 713(1):L6–L10, Apr. 2010. <https://doi.org/10.1088/2041-8205/713/1/L6>.
- J. Chae, H.-M. Park, K. Ahn, H. Yang, Y.-D. Park, K.-S. Cho, and W. Cao. Doppler Shifts of the H $\alpha$  Line and the Ca ii 854.2 nm Line in a Quiet Region of the Sun Observed with the FISS/NST. *SoPh*, 288(1):89–103, Nov. 2013. <https://doi.org/10.1007/s11207-013-0313-9>.
- J. Chae, H. Yang, H. Park, R. Ajar Maurya, K.-S. Cho, and V. Yurchyshyn. Superpenumbral Fibrils Powered by Sunspot Oscillations. *ApJ*, 789(2):108, July 2014. <https://doi.org/10.1088/0004-637X/789/2/108>.
- J. Chae, D. Song, M. Seo, K.-S. Cho, Y.-D. Park, and V. Yurchyshyn. Detection of Shock Merging in the Chromosphere of a Solar Pore. *ApJL*, 805(2):L21, June 2015. <https://doi.org/10.1088/2041-8205/805/2/L21>.
- J. Chae, J. Lee, K. Cho, D. Song, K. Cho, and V. Yurchyshyn. Photospheric Origin of Three-minute Oscillations in a Sunspot. *ApJ*, 836(1):18, Feb. 2017. <https://doi.org/10.3847/1538-4357/836/1/18>.

- J. Chae, M. S. Madjarska, H. Kwak, and K. Cho. Inference of chromospheric plasma parameters on the Sun. Multilayer spectral inversion of strong absorption lines. *A&A*, 640:A45, Aug. 2020. <https://doi.org/10.1051/0004-6361/202038141>.
- J. Chae, K. Cho, V. M. Nakariakov, K.-S. Cho, and R.-Y. Kwon. Spectroscopic Detection of Alfvénic Waves in the Chromosphere of Sunspot Regions. *ApJL*, 914(1):L16, June 2021. <https://doi.org/10.3847/2041-8213/ac052b>.
- Y. Chai, D. E. Gary, K. P. Reardon, and V. Yurchyshyn. A Study of Sunspot 3 Minute Oscillations Using ALMA and GST. *ApJ*, 924(2):100, Jan. 2022. <https://doi.org/10.3847/1538-4357/ac34f7>.
- Y. Chen, H. Tian, H. Peter, T. Samanta, V. Yurchyshyn, H. Wang, W. Cao, L. Wang, and J. He. Flame-like Ellerman Bombs and Their Connection to Solar Ultraviolet Bursts. *ApJL*, 875(2):L30, Apr. 2019. <https://doi.org/10.3847/2041-8213/ab18a4>.
- I.-H. Cho, V. M. Nakariakov, Y.-J. Moon, J.-Y. Lee, D. J. Yu, K.-S. Cho, V. Yurchyshyn, and H. Lee. Accelerating and Supersonic Density Fluctuations in Coronal Hole Plumes: Signature of Nascent Solar Winds. *ApJL*, 900(2):L19, Sept. 2020. <https://doi.org/10.3847/2041-8213/abb020>.
- K. Cho and J. Chae. Source Depth of Three-minute Umbral Oscillations. *ApJL*, 892(2):L31, Apr. 2020. <https://doi.org/10.3847/2041-8213/ab8295>.
- K. Cho, J. Lee, J. Chae, H. Wang, K. Ahn, H. Yang, E.-k. Lim, and R. A. Maurya. Strong Blue Asymmetry in H $\alpha$  Line as a Preflare Activity. *SoPh*, 291(8):2391–2406, Oct. 2016. <https://doi.org/10.1007/s11207-016-0963-5>.
- K. Cho, J. Chae, E.-k. Lim, and H. Yang. The Observational Evidence for the Internal Excitation of Sunspot Oscillations Inferred from the Fe I 5435 Å Line. *ApJ*, 879(2):67, July 2019a. <https://doi.org/10.3847/1538-4357/ab2466>.
- K. S. Cho, S. C. Bong, J. Chae, Y. H. Kim, Y. D. Park, and Y. Katsukawa. FISS Observations of Vertical Motion of Plasma in Tiny Pores. *SoPh*, 288(1):23–37, Nov. 2013. <https://doi.org/10.1007/s11207-012-0196-1>.
- K. S. Cho, S. C. Bong, V. M. Nakariakov, E. K. Lim, Y. D. Park, J. C. Chae, H. S. Yang, H. M. Park, and V. Yurchyshyn. Intensity and Doppler Velocity Oscillations in Pore Atmospheres. *ApJ*, 802(1):45, Mar. 2015. <https://doi.org/10.1088/0004-637X/802/1/45>.
- K.-S. Cho, I.-H. Cho, V. M. Nakariakov, V. B. Yurchyshyn, H. Yang, Y.-H. Kim, P. Kumar, and T. Magara. Oscillation of a Small H $\alpha$  Surge in a Solar Polar Coronal Hole. *ApJL*, 877(1):L1, May 2019b. <https://doi.org/10.3847/2041-8213/ab1eb5>.
- S. Şahin, V. Yurchyshyn, P. Kumar, A. Kilcik, K. Ahn, and X. Yang. Magnetic Field Dynamics and Varying Plasma Emission in Large-scale Coronal Loops. *ApJ*, 873(1):75, Mar. 2019. <https://doi.org/10.3847/1538-4357/ab04aa>.
- J. Deng, W. Song, D. Liu, Q. Li, G. Lin, and H. Wang. Improving the Spatial Resolution of Solar Images Using Generative Adversarial Network and Self-attention Mechanism. *ApJ*, 923(1):76, Dec. 2021. <https://doi.org/10.3847/1538-4357/ac2aa2>.
- N. Deng, V. Yurchyshyn, H. Tian, L. Kleint, C. Liu, Y. Xu, and H. Wang. Multi-wavelength Study of Transition Region Penumbra Subarcsecond Bright Dots Using IRIS and NST. *ApJ*, 829(2):103, Oct. 2016. <https://doi.org/10.3847/0004-637X/829/2/103>.
- C. Fang, Q. Hao, M.-D. Ding, and Z. Li. Can the temperature of Ellerman Bombs be more than 10 000 K? *Research in Astronomy and Astrophysics*, 17(4):031, Mar. 2017. <https://doi.org/10.1088/1674-4527/17/4/31>.
- Y. Gao, F. Li, B. Li, W. Cao, Y. Song, H. Tian, and M. Guo. Possible Signature of Sausage Waves in Photospheric Bright Points. *SoPh*, 296(12):184, Dec. 2021. <https://doi.org/10.1007/s11207-021-01928-9>.
- P. R. Goode, V. Yurchyshyn, W. Cao, V. Abramenko, A. Andic, K. Ahn, and J. Chae. Highest Resolution Observations of the Quietest Sun. *ApJL*, 714(1):L31–L35, May 2010. <https://doi.org/10.1088/2041-8205/714/1/L31>.
- P. R. Goode, V. Abramenko, and V. Yurchyshyn. New solar telescope in Big Bear: evidence for super-diffusivity and small-scale solar dynamos? *PhysS*, 86(1):018402, July 2012. <https://doi.org/10.1088/0031-8949/86/01/018402>.
- T. Gopalan Priya, J.-T. Su, J. Chen, Y.-Y. Deng, and D. Prasad Choudhury. Statistical analysis of dynamic fibrils observed from NST/BBSO observations. *Research in Astronomy and Astrophysics*, 18(2):017, Feb. 2018. <https://doi.org/10.1088/1674-4527/18/2/17>.
- Q. Hao, C. Fang, M. D. Ding, Z. Li, and W. Cao. Spectral Diagnostics of Solar Photospheric Bright Points. *ApJ*, 900(2):130, Sept. 2020. <https://doi.org/10.3847/1538-4357/aba692>.
- P. Hashim, Z.-X. Hong, H.-S. Ji, J.-H. Shen, K.-F. Ji, and W.-D. Cao. Observation of solar coronal heating powered by magneto-acoustic oscillations in a moss region. *Research in Astronomy and Astrophysics*, 21(4):105, May 2021. <https://doi.org/10.1088/1674-4527/21/4/105>.
- J. Hong, M. D. Ding, Y. Li, C. Fang, and W. Cao. Spectral Observations of Ellerman Bombs and Fitting with a Two-cloud Model. *ApJ*, 792(1):13, Sept. 2014. <https://doi.org/10.1088/0004-637X/792/1/13>.

- J. Hong, M. D. Ding, Y. Li, K. Yang, X. Cheng, F. Chen, C. Fang, and W. Cao. Bidirectional Outflows as Evidence of Magnetic Reconnection Leading to a Solar Microflare. *ApJL*, 820(1):L17, Mar. 2016. <https://doi.org/10.3847/2041-8205/820/1/L17>.
- J. Hong, M. D. Ding, and W. Cao. Multi-wavelength Spectral Analysis of Ellerman Bombs Observed by FISS and IRIS. *ApJ*, 838(2):101, Apr. 2017a. <https://doi.org/10.3847/1538-4357/aa671e>.
- Z. Hong, Y. Wang, and H. Ji. Quasiperiodic Microjets Driven by Granular Advection as Observed With High-resolution Imaging at He I 10830 Å. *ApJ*, 928(2):153, Apr. 2022. <https://doi.org/10.3847/1538-4357/ac590c>.
- Z.-X. Hong, X. Yang, Y. Wang, K.-F. Ji, H.-S. Ji, and W.-D. Cao. Location of energy source for coronal heating on the photosphere. *Research in Astronomy and Astrophysics*, 17(3):25, Feb. 2017b. <https://doi.org/10.1088/1674-4527/17/3/25>.
- N. Huang, Y. Xu, V. M. Sadykov, J. Jing, and H. Wang. Spectral Diagnosis of Mg II and H $\alpha$  Lines during the Initial Stage of an M6.5 Solar Flare. *ApJL*, 878(1):L15, June 2019. <https://doi.org/10.3847/2041-8213/ab2330>.
- N. Huang, V. M. Sadykov, Y. Xu, J. Jing, and H. Wang. Comparison of Enhanced Absorption in He I 10830 Å Observations and Modeling during the Early Phase of a Solar Flare. *ApJL*, 897(1):L6, July 2020. <https://doi.org/10.3847/2041-8213/ab9b7a>.
- H. Ji, P. Hashim, Z. Hong, Z. Xu, J. Shen, K. Ji, and W. Cao. Magneto-acoustic oscillations observed in a solar plage region. *Research in Astronomy and Astrophysics*, 21(7):179, Aug. 2021. <https://doi.org/10.1088/1674-4527/21/7/179>.
- H. Jiang, J. Jing, J. Wang, C. Liu, Q. Li, Y. Xu, J. T. L. Wang, and H. Wang. Tracing H $\alpha$  Fibrils through Bayesian Deep Learning. *ApJS*, 256(1):20, Sept. 2021. <https://doi.org/10.3847/1538-4365/ac14b7>.
- H. Jiang, Q. Li, Y. Xu, W. Hsu, K. Ahn, W. Cao, J. T. L. Wang, and H. Wang. Inferring Line-of-sight Velocities and Doppler Widths from Stokes Profiles of GST/NIRIS Using Stacked Deep Neural Networks. *ApJ*, 939(2):66, Nov. 2022. <https://doi.org/10.3847/1538-4357/ac927e>.
- J. Jing, Y. Xu, W. Cao, C. Liu, D. Gary, and H. Wang. Unprecedented Fine Structure of a Solar Flare Revealed by the 1.6 m New Solar Telescope. *Scientific Reports*, 6:24319, Apr. 2016. <https://doi.org/10.1038/srep24319>.
- J. Jing, Q. Li, C. Liu, J. Lee, Y. Xu, W. Cao, and H. Wang. High-resolution Observations of Dynamics of Superpenumbral H $\alpha$  Fibrils. *ApJ*, 880(2):143, Aug. 2019. <https://doi.org/10.3847/1538-4357/ab2b44>.
- A. D. Joshi, Y. Hanaoka, Y. Suematsu, S. Morita, V. Yurchyshyn, and K.-S. Cho. Pre-eruption Oscillations in Thin and Long Features in a Quiescent Filament. *ApJ*, 833(2):243, Dec. 2016. <https://doi.org/10.3847/1538-4357/833/2/243>.
- J. Kang, J. Chae, V. M. Nakariakov, K. Cho, H. Kwak, and K. Lee. The Physical Nature of Spiral Wave Patterns in Sunspots. *ApJL*, 877(1):L9, May 2019. <https://doi.org/10.3847/2041-8213/ab1f6c>.
- A. Kilcik, V. B. Yurchyshyn, M. Rempel, V. Abramenko, R. Kitai, P. R. Goode, W. Cao, and H. Watanabe. Properties of Umbral Dots as Measured from the New Solar Telescope Data and MHD Simulations. *ApJ*, 745(2):163, Feb. 2012. <https://doi.org/10.1088/0004-637X/745/2/163>.
- A. Kilcik, V. Sarp, V. Yurchyshyn, J.-P. Rozelot, and A. Ozguc. Physical Characteristics of Umbral Dots Derived from a High-Resolution Observations. *SoPh*, 295(4):58, Apr. 2020. <https://doi.org/10.1007/s11207-020-01618-y>.
- Y.-H. Kim, V. Yurchyshyn, S.-C. Bong, I.-H. Cho, K.-S. Cho, J. Lee, E.-K. Lim, Y.-D. Park, H. Yang, K. Ahn, P. R. Goode, and B.-H. Jang. Simultaneous observation of a hot explosion by NST and IRIS. *ApJ*, 810(1):38, Sept. 2015. <https://doi.org/10.1088/0004-637X/810/1/38>.
- I. N. Kitiashvili, V. I. Abramenko, P. R. Goode, A. G. Kosovichev, S. K. Lele, N. N. Mansour, A. A. Wray, and V. B. Yurchyshyn. Turbulent kinetic energy spectra of solar convection from New Solar Telescope observations and realistic magnetohydrodynamic simulations. *Physica Scripta Volume T*, 155:014025, July 2013. <https://doi.org/10.1088/0031-8949/2013/T155/014025>.
- P. Kumar, V. Yurchyshyn, H. Wang, and K.-S. Cho. Formation and Eruption of a Small Flux Rope in the Chromosphere Observed by NST, IRIS, and SDO. *ApJ*, 809(1):83, Aug. 2015. <https://doi.org/10.1088/0004-637X/809/1/83>.
- P. Kumar, V. Yurchyshyn, K.-S. Cho, and H. Wang. Multiwavelength observations of a flux rope formation by series of magnetic reconnection in the chromosphere. *A&A*, 603:A36, July 2017. <https://doi.org/10.1051/0004-6361/201629295>.
- H. Kwak, J. Chae, D. Song, Y.-H. Kim, E.-K. Lim, and M. S. Madjarska. Oscillatory Response of the Solar Chromosphere to a Strong Downflow Event above a Sunspot. *ApJL*, 821(2):L30, Apr. 2016. <https://doi.org/10.3847/2041-8205/821/2/L30>.

- H. Kwak, J. Chae, M. S. Madjarska, K. Cho, and D. Song. Impulsive wave excitation by rapidly changing granules. *A&A*, 642:A154, Oct. 2020. <https://doi.org/10.1051/0004-6361/202038288>.
- J. Lee, V. Yurchyshyn, H. Wang, X. Yang, W. Cao, and J. Carlos Martínez Oliveros. Solar Chromospheric Network as a Source for Solar Wind Switchbacks. *ApJL*, 935(2):L27, Aug. 2022. <https://doi.org/10.3847/2041-8213/ac86bf>.
- F. Lepreti, V. Carbone, V. I. Abramenko, V. Yurchyshyn, P. R. Goode, V. Capparelli, and A. Vecchio. Turbulent Pair Dispersion of Photospheric Bright Points. *ApJL*, 759(1):L17, Nov. 2012. <https://doi.org/10.1088/2041-8205/759/1/L17>.
- D. Li, X. Yang, X. Y. Bai, J. T. Su, Z. J. Ning, W. Cao, and Y. Y. Deng. Doppler shift oscillations of a sunspot detected by CYRA and IRIS. *A&A*, 642:A231, Oct. 2020. <https://doi.org/10.1051/0004-6361/202039007>.
- Q. Li, N. Deng, J. Jing, and H. Wang. High-resolution Observations of Downflows at One End of a Pre-eruption Filament. *ApJ*, 841(2):112, June 2017. <https://doi.org/10.3847/1538-4357/aa6faa>.
- Q. Li, X. Yan, J. Wang, D. Kong, Z. Xue, L. Yang, and W. Cao. The Formation of a Sunspot Penumbra Sector in Active Region NOAA 12574. *ApJ*, 857(1):21, Apr. 2018. <https://doi.org/10.3847/1538-4357/aab6b0>.
- Q. Li, N. Deng, J. Jing, C. Liu, and H. Wang. High-resolution Observation of Moving Magnetic Features. *ApJ*, 876(2):129, May 2019. <https://doi.org/10.3847/1538-4357/ab18aa>.
- Z. Li, C. Fang, Y. Guo, P.-F. Chen, Z. Xu, and W.-D. Cao. Diagnostics of Ellerman bombs with high-resolution spectral data. *Research in Astronomy and Astrophysics*, 15(9):1513, Sept. 2015. <https://doi.org/10.1088/1674-4527/15/9/008>.
- Z. Li, C. Fang, Y. Guo, P. F. Chen, P. Zou, and W. Cao. High-resolution Observations of a Large Fan-shaped Surge. *ApJ*, 826(2):217, Aug. 2016. <https://doi.org/10.3847/0004-637X/826/2/217>.
- B. Liang, X. Chen, L. Yu, S. Feng, Y. Guo, W. Cao, W. Dai, Y. Yang, and D. Yuan. High-precision Multichannel Solar Image Registration Using Image Intensity. *ApJS*, 261(2):10, Aug. 2022. <https://doi.org/10.3847/1538-4365/ac7232>.
- E.-K. Lim, V. Yurchyshyn, V. Abramenko, K. Ahn, W. Cao, and P. Goode. Photospheric Signatures of Granular-scale Flux Emergence and Cancellation at the Penumbra Boundary. *ApJ*, 740(2):82, Oct. 2011. <https://doi.org/10.1088/0004-637X/740/2/82>.
- E.-K. Lim, V. Yurchyshyn, and P. Goode. First Simultaneous Detection of Moving Magnetic Features in Photospheric Intensity and Magnetic Field Data. *ApJ*, 753(1):89, July 2012. <https://doi.org/10.1088/0004-637X/753/1/89>.
- E.-K. Lim, V. Yurchyshyn, P. Goode, and K.-S. Cho. Observation of a Non-radial Penumbra in a Flux Emerging Region under Chromospheric Canopy Fields. *ApJL*, 769(1):L18, May 2013. <https://doi.org/10.1088/2041-8205/769/1/L18>.
- E.-K. Lim, V. Yurchyshyn, S.-H. Park, S. Kim, K.-S. Cho, P. Kumar, J. Chae, H. Yang, K. Cho, D. Song, and Y.-H. Kim. Observations of a Series of Flares and Associated Jet-like Eruptions Driven by the Emergence of Twisted Magnetic Fields. *ApJ*, 817(1):39, Jan. 2016. <https://doi.org/10.3847/0004-637X/817/1/39>.
- E.-K. Lim, H. Yang, V. Yurchyshyn, J. Chae, D. Song, and M. S. Madjarska. Detection of Opposite Magnetic Polarity in a Light Bridge: Its Emergence and Cancellation in Association with LB Fan-shaped Jets. *ApJ*, 904(2):84, Dec. 2020. <https://doi.org/10.3847/1538-4357/abc1e0>.
- C. Liu, Y. Xu, W. Cao, N. Deng, J. Lee, H. S. Hudson, D. E. Gary, J. Wang, J. Jing, and H. Wang. Flare differentially rotates sunspot on Sun's surface. *Nature Communications*, 7:13104, Oct. 2016. <https://doi.org/10.1038/ncomms13104>.
- C. Liu, W. Cao, J. Chae, K. Ahn, D. Prasad Choudhary, J. Lee, R. Liu, N. Deng, J. Wang, and H. Wang. Evolution of Photospheric Vector Magnetic Field Associated with Moving Flare Ribbons as Seen by GST. *ApJ*, 869(1):21, Dec. 2018. <https://doi.org/10.3847/1538-4357/aaecd0>.
- H. Liu, Y. Xu, J. Wang, J. Jing, C. Liu, J. T. L. Wang, and H. Wang. Inferring Vector Magnetic Fields from Stokes Profiles of GST/NIRIS Using a Convolutional Neural Network. *ApJ*, 894(1):70, May 2020. <https://doi.org/10.3847/1538-4357/ab8818>.
- Y. Liu, C. Jiang, D. Yuan, P. Zuo, Y. Wang, and W. Cao. Investigations of Sizes and Dynamical Motions of Solar Photospheric Granules by a Novel Granular Segmenting Algorithm. *ApJ*, 923(2):133, Dec. 2021. <https://doi.org/10.3847/1538-4357/ac2dfd>.
- Y. Liu, G. P. Ruan, B. Schmieder, S. Masson, Y. Chen, J. T. Su, B. Wang, X. Y. Bai, Y. Su, and W. Cao. Fan-shaped jet close to a light bridge. *A&A*, 667:A24, Nov. 2022a. <https://doi.org/10.1051/0004-6361/202243292>.

- Y.-X. Liu, C.-W. Jiang, D. Yuan, P.-B. Zuo, and W.-D. Cao. Length Scale of Photospheric Granules in Solar Active Regions. *Research in Astronomy and Astrophysics*, 22(8):085008, Aug. 2022b. <https://doi.org/10.1088/1674-4527/ac7518>.
- V. Lozitsky, V. Yurchyshyn, K. Ahn, and H. Wang. Observations of Extremely Strong Magnetic Fields in Active Region NOAA 12673 Using GST Magnetic Field Measurement. *ApJ*, 928(1):41, Mar. 2022. <https://doi.org/10.3847/1538-4357/ac5518>.
- V. G. Lozitsky, V. B. Yurchyshyn, K. Ahn, H. Wang, and N. I. Lozitska. Problem of Super-Strong Magnetic Fields on the Sun: Brief Chronology and New Observational Data. *Odessa Astronomical Publications*, 30:152, Jan. 2018. <https://doi.org/10.18524/1810-4215.2018.31.144560>.
- M. S. Madjarska, J. Chae, F. Moreno-Insertis, Z. Hou, D. Nóbrega-Siverio, H. Kwak, K. Galsgaard, and K. Cho. The chromospheric component of coronal bright points. Coronal and chromospheric responses to magnetic-flux emergence. *A&A*, 646:A107, Feb. 2021. <https://doi.org/10.1051/0004-6361/202039329>.
- R. A. Maurya, J. Chae, H. Park, H. Yang, D. Song, and K. Cho. Chromospheric Sunspot Oscillations in H $\alpha$  and Ca ii 8542 Å. *SoPh*, 288(1):73–88, Nov. 2013. <https://doi.org/10.1007/s11207-013-0286-8>.
- H. Park, J. Chae, D. Song, R. A. Maurya, H. Yang, Y.-D. Park, B.-H. Jang, J. Nah, K.-S. Cho, Y.-H. Kim, K. Ahn, W. Cao, and P. R. Goode. Temperature of Solar Prominences Obtained with the Fast Imaging Solar Spectrograph on the 1.6 m New Solar Telescope at the Big Bear Solar Observatory. *SoPh*, 288(1):105–116, Nov. 2013. <https://doi.org/10.1007/s11207-013-0271-2>.
- T. G. Priya, C. Wenda, S. Jiangtao, C. Jie, M. Xinjie, D. Yuanyong, and E. Robert. Observations of Running Penumbra Waves Emerging in a Sunspot. *ApJ*, 852(1):15, Jan. 2018. <https://doi.org/10.3847/1538-4357/aa9c47>.
- T. Samanta, H. Tian, V. Yurchyshyn, H. Peter, W. Cao, A. Sterling, R. Erdélyi, K. Ahn, S. Feng, D. Utz, D. Banerjee, and Y. Chen. Generation of solar spicules and subsequent atmospheric heating. *Science*, 366(6467):890–894, Nov. 2019. <https://doi.org/10.1126/science.aaw2796>.
- D. Schmidt, N. Gorceix, and P. Goode. On the sequence of deformable mirrors in MCAO: findings from an on-sky, closed-loop experiment. In *Society of Photo-Optical Instrumentation Engineers (SPIE) Conference Series*, volume 11448 of *Society of Photo-Optical Instrumentation Engineers (SPIE) Conference Series*, page 1144842, Dec. 2020. <https://doi.org/10.1117/12.2563376>.
- M. Seo, C. Quintero Noda, J. Lee, and J. Chae. Depth of Ellerman Burst Derived from High-resolution H $\alpha$  and Ca II 8542 Å Spectra. *ApJ*, 871(1):125, Jan. 2019. <https://doi.org/10.3847/1538-4357/aaf55f>.
- I. N. Sharykin and A. G. Kosovichev. Fine Structure of Flare Ribbons and Evolution of Electric Currents. *ApJL*, 788(1):L18, June 2014. <https://doi.org/10.1088/2041-8205/788/1/L18>.
- I. N. Sharykin, V. M. Sadykov, A. G. Kosovichev, S. Vargas-Dominguez, and I. V. Zimovets. Flare Energy Release in the Lower Solar Atmosphere near the Magnetic Field Polarity Inversion Line. *ApJ*, 840(2):84, May 2017. <https://doi.org/10.3847/1538-4357/aa6dfd>.
- J. Shen, H. Ji, and Y. Su. The Precursor Phase of an X-class Flare: Magnetic Reconnection, Powering and Non-thermal Electrons. *Research in Astronomy and Astrophysics*, 22(1):015019, Jan. 2022. <https://doi.org/10.1088/1674-4527/ac389b>.
- D. Song, J. Chae, S. Park, K.-S. Cho, E.-K. Lim, K. Ahn, and W. Cao. Detection of a Fine-scale Discontinuity of Photospheric Magnetic Fields Associated with Solar Coronal Loop Brightenings. *ApJL*, 810(2):L16, Sept. 2015. <https://doi.org/10.1088/2041-8205/810/2/L16>.
- D. Song, J. Chae, H. Kwak, R. Kano, V. Yurchyshyn, Y.-J. Moon, E.-K. Lim, and J. Lee. Three-minute Sunspot Oscillations Driven by Magnetic Reconnection in a Light Bridge. *ApJL*, 850(2):L33, Dec. 2017a. <https://doi.org/10.3847/2041-8213/aa9a36>.
- D. Song, J. Chae, V. Yurchyshyn, E.-K. Lim, K.-S. Cho, H. Yang, K. Cho, and H. Kwak. Chromospheric Plasma Ejections in a Light Bridge of a Sunspot. *ApJ*, 835(2):240, Feb. 2017b. <https://doi.org/10.3847/1538-4357/835/2/240>.
- A. C. Sterling, R. L. Moore, T. Samanta, and V. Yurchyshyn. Possible Production of Solar Spicules by Microfilament Eruptions. *ApJL*, 893(2):L45, Apr. 2020. <https://doi.org/10.3847/2041-8213/ab86a5>.
- J. T. Su, K. F. Ji, D. Banerjee, W. D. Cao, T. G. Priya, J. S. Zhao, S. J. Yu, H. S. Ji, and M. Zhang. Interference of the Running Waves at Light Bridges of a Sunspot. *ApJ*, 816(1):30, Jan. 2016a. <https://doi.org/10.3847/0004-637X/816/1/30>.

- J. T. Su, K. F. Ji, W. Cao, D. Banerjee, T. G. Priya, J. S. Zhao, X. Y. Bai, J. Chen, M. Zhang, and H. S. Ji. Observations of Oppositely Directed Umbral Wavefronts Rotating in Sunspots Obtained from the New Solar Telescope of BBSO. *ApJ*, 817(2):117, Feb. 2016b. <https://doi.org/10.3847/0004-637X/817/2/117>.
- Y. Su, R. Liu, S. Li, W. Cao, K. Ahn, and H. Ji. High-resolution Observations of Flares in an Arch Filament System. *ApJ*, 855(2):77, Mar. 2018. <https://doi.org/10.3847/1538-4357/aaac31>.
- R. Sych, Y. Zhugzhda, and X. Yan. Properties of Local Oscillations in the Lower Sunspot Atmosphere. *ApJ*, 888(2):84, Jan. 2020. <https://doi.org/10.3847/1538-4357/ab5a78>.
- H. Tian, V. Yurchyshyn, H. Peter, S. K. Solanki, P. R. Young, L. Ni, W. Cao, K. Ji, Y. Zhu, J. Zhang, T. Samanta, Y. Song, J. He, L. Wang, and Y. Chen. Frequently Occurring Reconnection Jets from Sunspot Light Bridges. *ApJ*, 854(2):92, Feb. 2018. <https://doi.org/10.3847/1538-4357/aaa89d>.
- S. Toriumi and H. Wang. Flare-productive active regions. *Living Reviews in Solar Physics*, 16(1):3, May 2019. <https://doi.org/10.1007/s41116-019-0019-7>.
- S. Vargas Domínguez, A. Kosovichev, and V. Yurchyshyn. Multi-wavelength High-resolution Observations of a Small-scale Emerging Magnetic Flux Event and the Chromospheric and Coronal Response. *ApJ*, 794(2):140, Oct. 2014. <https://doi.org/10.1088/0004-637X/794/2/140>.
- S. Vargas Dominguez, A. G. Kosovichev, and V. Yurchyshyn. Emergence of a small-scale magnetic flux tube and the response of the solar atmosphere. *Central European Astrophysical Bulletin*, 38:25–30, Jan. 2014.
- H. Wang and C. Liu. Signatures of Magnetic Flux Ropes in the Low Solar Atmosphere Observed in High Resolution. *Frontiers in Astronomy and Space Sciences*, 6:18, Apr. 2019. <https://doi.org/10.3389/fspas.2019.00018>.
- H. Wang, C. Liu, K. Ahn, Y. Xu, J. Jing, N. Deng, N. Huang, R. Liu, K. Kusano, G. D. Fleishman, D. E. Gary, and W. Cao. High-resolution observations of flare precursors in the low solar atmosphere. *Nature Astronomy*, 1:0085, Mar. 2017. <https://doi.org/10.1038/s41550-017-0085>.
- H. Wang, R. Liu, Q. Li, C. Liu, N. Deng, Y. Xu, J. Jing, Y. Wang, and W. Cao. Extending Counter-streaming Motion from an Active Region Filament to a Sunspot Light Bridge. *ApJL*, 852(1):L18, Jan. 2018a. <https://doi.org/10.3847/2041-8213/aaa2f4>.
- H. Wang, V. Yurchyshyn, C. Liu, K. Ahn, S. Toriumi, and W. Cao. Strong Transverse Photosphere Magnetic Fields and Twist in Light Bridge Dividing Delta Sunspot of Active Region 12673. *Research Notes of the American Astronomical Society*, 2(1):8, Jan. 2018b. <https://doi.org/10.3847/2515-5172/aaa670>.
- J. Wang, C. Liu, N. Deng, and H. Wang. Evolution of Photospheric Flow and Magnetic Fields Associated with the 2015 June 22 M6.5 Flare. *ApJ*, 853(2):143, Feb. 2018c. <https://doi.org/10.3847/1538-4357/aaa712>.
- J. Wang, X. Yan, Z. Qu, S. UeNo, K. Ichimoto, L. Deng, W. Cao, and Z. Liu. Formation of an Active Region Filament Driven By a Series of Jets. *ApJ*, 863(2):180, Aug. 2018d. <https://doi.org/10.3847/1538-4357/aad187>.
- J. Wang, C. Liu, W. Cao, and H. Wang. High-resolution Observations of Small-scale Flux Emergence by GST. *ApJ*, 900(1):84, Sept. 2020a. <https://doi.org/10.3847/1538-4357/aba696>.
- J. Wang, J. Lee, C. Liu, W. Cao, and H. Wang. A High-resolution Study of Magnetic Field Evolution and Spicular Activity around the Boundary of a Coronal Hole. *ApJ*, 924(2):137, Jan. 2022. <https://doi.org/10.3847/1538-4357/ac374e>.
- Y. Wang, Y. Su, Z. Hong, Z. Zeng, K. Ji, P. R. Goode, W. Cao, and H. Ji. High Resolution He I 10830 AA Narrow-band Imaging of an M-class Flare. I - Analysis of Sunspot Dynamics during Flaring. *ApJ*, 833(2):250, Dec. 2016. <https://doi.org/10.3847/1538-4357/833/2/250>.
- Y. Wang, Y. Su, J. Shen, X. Yang, W. Cao, and H. Ji. High-resolution He I 10830 Å Narrowband Imaging for an M-class Flare. II. Multiple Hot Channels: Their Origin and Destination. *ApJ*, 859(2):148, June 2018e. <https://doi.org/10.3847/1538-4357/aac0f7>.
- Y. Wang, H. Ji, A. Warmuth, Y. Li, and W. Cao. High-resolution He I 10830 Å Narrowband Imaging for an M-class Flare. III. EUV Late Phase. *ApJ*, 905(2):126, Dec. 2020b. <https://doi.org/10.3847/1538-4357/abc47a>.
- Y. Wang, Q. Zhang, and H. Ji. High-resolution He I 10830 Å Narrowband Imaging for a Small-scale Chromospheric Jet. *ApJ*, 913(1):59, May 2021. <https://doi.org/10.3847/1538-4357/abf2b9>.
- Y. Wei, B. Chen, S. Yu, H. Wang, J. Jing, and D. E. Gary. Coronal Magnetic Field Measurements along a Partially Erupting Filament in a Solar Flare. *ApJ*, 923(2):213, Dec. 2021. <https://doi.org/10.3847/1538-4357/ac2f99>.
- L. Xu, Y. Yang, Y. Yan, Y. Zhang, X. Bai, B. Liang, W. Dai, S. Feng, and W. Cao. Research on Multiwavelength Isolated Bright Points Based on Deep Learning. *ApJ*, 911(1):32, Apr. 2021. <https://doi.org/10.3847/1538-4357/abe705>.

- Y. Xu, W. Cao, M. Ding, L. Kleint, J. Su, C. Liu, H. Ji, J. Chae, J. Jing, K. Cho, K. Cho, D. Gary, and H. Wang. Ultra-narrow Negative Flare Front Observed in Helium-10830 Å Using the 1.6 m New Solar Telescope. *ApJ*, 819(2):89, Mar. 2016. <https://doi.org/10.3847/0004-637X/819/2/89>.
- Y. Xu, W. Cao, K. Ahn, J. Jing, C. Liu, J. Chae, N. Huang, N. Deng, D. E. Gary, and H. Wang. Transient rotation of photospheric vector magnetic fields associated with a solar flare. *Nature Communications*, 9:46, Jan. 2018. <https://doi.org/10.1038/s41467-017-02509-w>.
- Y. Xu, X. Yang, G. S. Kerr, V. Polito, V. M. Sadykov, J. Jing, W. Cao, and H. Wang. Multi-passband Observations of a Solar Flare over the He I 10830 Å line. *ApJL*, 924(1):L18, Jan. 2022. <https://doi.org/10.3847/2041-8213/ac447c>.
- X. L. Yan, C. W. Jiang, Z. K. Xue, J. C. Wang, E. R. Priest, L. H. Yang, D. F. Kong, W. D. Cao, and H. S. Ji. The Eruption of a Small-scale Emerging Flux Rope as the Driver of an M-class Flare and of a Coronal Mass Ejection. *ApJ*, 845(1):18, Aug. 2017. <https://doi.org/10.3847/1538-4357/aa7e29>.
- H. Yang, J. Chae, E.-K. Lim, H. Park, K. Cho, R. A. Mauitya, D. Song, Y.-H. Kim, and P. R. Goode. Velocities and Temperatures of an Ellerman Bomb and Its Associated Features. *SoPh*, 288(1):39–53, Nov. 2013. <https://doi.org/10.1007/s11207-013-0354-0>.
- H. Yang, J. Chae, E.-K. Lim, K.-s. Lee, H. Park, D.-u. Song, and K. Cho. Magnetic-reconnection Generated Shock Waves as a Driver of Solar Surges. *ApJL*, 790(1):L4, July 2014. <https://doi.org/10.1088/2041-8205/790/1/L4>.
- H. Yang, J. Chae, E.-K. Lim, D. Song, K. Cho, H. Kwak, V. B. Yurchyshyn, and Y.-H. Kim. Fine-scale Photospheric Connections of Ellerman Bombs. *ApJ*, 829(2):100, Oct. 2016. <https://doi.org/10.3847/0004-637X/829/2/100>.
- H. Yang, E.-K. Lim, H. Iijima, V. Yurchyshyn, K.-S. Cho, J. Lee, B. Schmieder, Y.-H. Kim, S. Kim, and S.-C. Bong. Vortex Formations and Its Associated Surges in a Sunspot Light Bridge. *ApJ*, 882(2):175, Sept. 2019a. <https://doi.org/10.3847/1538-4357/ab36b7>.
- M. Yang, Y. Tian, Y. Liu, and C. Rao. Automated Solar Flare Detection and Feature Extraction in High-Resolution and Full-Disk H $\alpha$  Images. *SoPh*, 293(5): 81, May 2018. <https://doi.org/10.1007/s11207-018-1300-y>.
- M. Yang, X. Gong, Y. Liu, Y. Tian, and C. Rao. Automated Recognition of Post-Flare Loops in High-Resolution H $\alpha$  Red-Wing Images. *SoPh*, 297(5):62, May 2022a. <https://doi.org/10.1007/s11207-022-01993-8>.
- X. Yang, W. Cao, H. Ji, P. Hashim, and J. Shen. High-resolution Spectroscopic Imaging of Counter-streaming Motions in Solar Active Region Magnetic Loops. *ApJL*, 881(1):L25, Aug. 2019b. <https://doi.org/10.3847/2041-8213/ab365b>.
- X. Yang, V. Yurchyshyn, K. Ahn, M. Penn, and W. Cao. Light Bridge Brightening and Plasma Ejection Driven by a Magnetic Flux Emergence Event. *ApJ*, 886(1):64, Nov. 2019c. <https://doi.org/10.3847/1538-4357/ab4a7d>.
- X. Yang, W. Cao, N. Gorceix, C. Plymate, S. Shumoko, X. Bai, M. Penn, T. Ayres, R. Coulter, and P. R. Goode. CYRA: the cryogenic infrared spectrograph for the Goode Solar Telescope in Big Bear. In *Society of Photo-Optical Instrumentation Engineers (SPIE) Conference Series*, volume 11447 of *Society of Photo-Optical Instrumentation Engineers (SPIE) Conference Series*, page 11447AG, Dec. 2020. <https://doi.org/10.1117/12.2562474>.
- X. Yang, W. Cao, and V. Yurchyshyn. GST Data-processing Workflow: Image Registration and Alignment. *ApJS*, 262(2):55, Oct. 2022b. <https://doi.org/10.3847/1538-4365/ac91c9>.
- V. Yurchyshyn, V. Abramenko, and P. Goode. Dynamics of Chromospheric Upflows and Underlying Magnetic Fields. *ApJ*, 767(1):17, Apr. 2013. <https://doi.org/10.1088/0004-637X/767/1/17>.
- V. Yurchyshyn, V. Abramenko, A. Kosovichev, and P. Goode. High Resolution Observations of Chromospheric Jets in Sunspot Umbra. *ApJ*, 787(1):58, May 2014. <https://doi.org/10.1088/0004-637X/787/1/58>.
- V. Yurchyshyn, V. Abramenko, and A. Kilcik. Dynamics in Sunspot Umbra as Seen in New Solar Telescope and Interface Region Imaging Spectrograph Data. *ApJ*, 798(2):136, Jan. 2015a. <https://doi.org/10.1088/0004-637X/798/2/136>.
- V. Yurchyshyn, P. Kumar, K. S. Cho, E. K. Lim, and V. I. Abramenko. Multiwavelength Observations of a Slow-rise, Multistep X1.6 Flare and the Associated Eruption. *ApJ*, 812(2):172, Oct. 2015b. <https://doi.org/10.1088/0004-637X/812/2/172>.
- V. Yurchyshyn, P. Kumar, V. Abramenko, Y. Xu, P. R. Goode, K. S. Cho, and E. K. Lim. High-resolution Observations of a White-light Flare with NST. *ApJ*, 838(1):32, Mar. 2017. <https://doi.org/10.3847/1538-4357/aa633f>.

- V. Yurchyshyn, W. Cao, V. Abramenko, X. Yang, and K.-S. Cho. Rapid Evolution of Type II Spicules Observed in Goode Solar Telescope On-disk  $H_{\alpha}$  Images. *ApJL*, 891(1):L21, Mar. 2020a. <https://doi.org/10.3847/2041-8213/ab7931>.
- V. Yurchyshyn, A. Kilcik, S. Şahin, V. Abramenko, and E.-K. Lim. Spatial Distribution of the Origin of Umbral Waves in a Sunspot Umbra. *ApJ*, 896(2):150, June 2020b. <https://doi.org/10.3847/1538-4357/ab91b8>.
- V. B. Yurchyshyn, P. R. Goode, V. I. Abramenko, J. Chae, W. Cao, A. Andic, and K. Ahn. Chromospheric Signatures of Small-scale Flux Emergence as Observed with New Solar Telescope and Hinode Instruments. *ApJ*, 722(2):1970–1976, Oct. 2010. <https://doi.org/10.1088/0004-637X/722/2/1970>.
- V. B. Yurchyshyn, P. R. Goode, V. I. Abramenko, and O. Steiner. On the Origin of Intergranular Jets. *ApJL*, 736(2):L35, Aug. 2011. <https://doi.org/10.1088/2041-8205/736/2/L35>.
- Z. Zeng, J. Qiu, W. Cao, and P. G. Judge. A Flare Observed in Coronal, Transition Region, and Helium I 10830 Å Emissions. *ApJ*, 793(2):87, Oct. 2014. <https://doi.org/10.1088/0004-637X/793/2/87>.
- Z. Zeng, B. Chen, H. Ji, P. R. Goode, and W. Cao. Resolving the Fan-spine Reconnection Geometry of a Small-scale Chromospheric Jet Event with the New Solar Telescope. *ApJL*, 819(1):L3, Mar. 2016. <https://doi.org/10.3847/2041-8205/819/1/L3>.
- J. Zhang, H. Tian, S. K. Solanki, H. Wang, H. Peter, K. Ahn, Y. Xu, Y. Zhu, W. Cao, J. He, and L. Wang. Dark Structures in Sunspot Light Bridges. *ApJ*, 865(1):29, Sept. 2018. <https://doi.org/10.3847/1538-4357/aada0a>.
- J. Zhao, T. Felipe, R. Chen, and E. Khomenko. Tracing p-mode Waves from the Photosphere to the Corona in Active Regions. *ApJL*, 830(1):L17, Oct. 2016. <https://doi.org/10.3847/2041-8205/830/1/L17>.
- J. Zhao, J. Su, X. Yang, H. Li, B. Schmieder, K. Ahn, and W. Cao. Chromospheric Recurrent Jets in a Sunspot Group and Their Intergranular Origin. *ApJ*, 932(2):95, June 2022. <https://doi.org/10.3847/1538-4357/ac6e3b>.
- R. Zheng, Y. Chen, B. Wang, H. Song, and W. Cao. Formation of a tiny flux rope in the center of an active region driven by magnetic flux emergence, convergence, and cancellation. *A&A*, 642:A199, Oct. 2020. <https://doi.org/10.1051/0004-6361/202037475>.
- P. Zou, C. Fang, P. F. Chen, K. Yang, Q. Hao, and W. Cao. Material Supply and Magnetic Configuration of an Active Region Filament. *ApJ*, 831(2):123, Nov. 2016. <https://doi.org/10.3847/0004-637X/831/2/123>.
- P. Zou, C.-W. Jiang, F.-S. Wei, and W.-D. Cao. Can an injection model replenish filaments in a weak magnetic environment? *Research in Astronomy and Astrophysics*, 19(6):084, June 2019. <https://doi.org/10.1088/1674-4527/19/6/84>.
- Z. H. Zuo, Y. Li, J. H. Sha, and T. H. Zhou. A Solar Jet Triggered by a Decaying Satellite Sunspot. *Acta Astronomica Sinica*, 60(6):56, Nov. 2019.